AD-A072 560   SPERRY UNIVAC ST PAUL MINN APPLIED PHYSICS LAB   F/G 17/5
LASER DEFLECTION ANALYSIS.(U)
MAY 79 F G HEWITT, G L NELSON, J A KRAWEZAK   F33615-77-C-1163
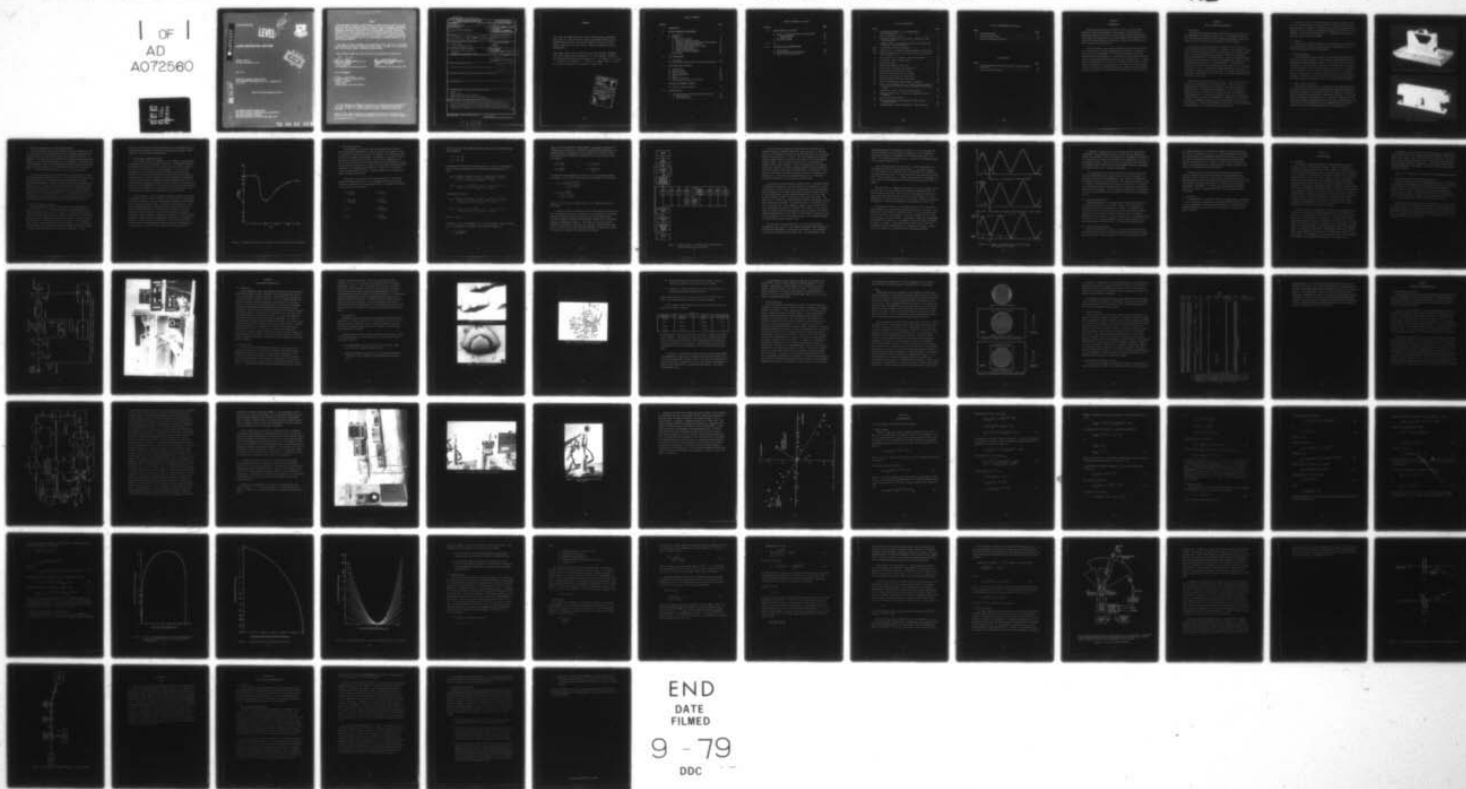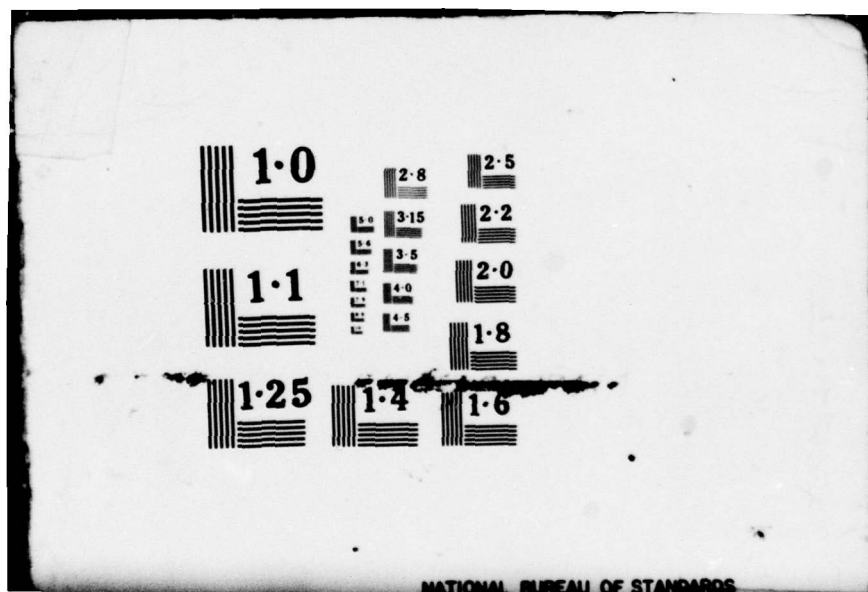AFAL-TR-78-193

UNCLASSIFIED   NL

1 OF 1
AD
A072560

END
DATE
FILMED
9 - 79
DDC

AFAL-TR-78-193

LEVEL

LASER DEFELECTOR ANALYSIS

SPERRY UNIVAC
ST. PAUL, MINNESOTA 55165

MAY 1979

TECHNICAL REPORT AFAL-TR-78-193
FINAL REPORT FOR PERIOD JULY 1977 - AUGUST 1978

AIR FORCE AVIONICS LABORATORY
AIR FORCE WRIGHT AERONAUTICAL LABORATORIES
AIR FORCE SYSTEMS COMMAND
WRIGHT-PATTERSON AIR FORCE BASE, OHIO 45433

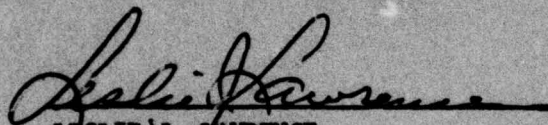79 08 03 022
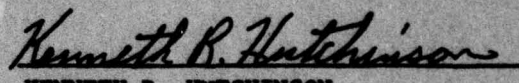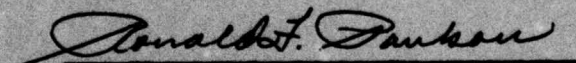
This technical report has been reviewed and is approved for publication.

LESLIE J. LAWRENCE
Project Engineer
E-O Techniques and Applications Grp

KENNETH R. HUTCHINSON
Chief
E-O Techniques and Applications Grp

FOR THE COMMANDER

RONALD F. PAULSON
Acting Chief
Electro-Optics Technology Branch

REPORT DOCUMENTATION PAGE		READ INSTRUCTIONS BEFORE COMPLETING FORM
1. REPORT NUMBER AFAL-TR-78-193	2. GOVT ACCESSION NO.	3. RECIPIENT'S CATALOG NUMBER
4. TITLE (and Subtitle) Laser Deflector Analysis		5. TYPE OF REPORT & PERIOD COVERED Technical July 1977 — August 1978
		6. PERFORMING ORG. REPORT NUMBER
7. AUTHOR(s) F. G. Hewitt, G. L. Nelson, and J.A. Krawezak		8. CONTRACT OR GRANT NUMBER(s) F33615-77-C-1163
9. PERFORMING ORGANIZATION NAME AND ADDRESS Sperry Univac St. Paul, Minnesota 55165		10. PROGRAM ELEMENT, PROJECT, TASK AREA A WORK UNIT NUMBERS 62204F 20010245
11. CONTROLLING OFFICE NAME AND ADDRESS Air Force Avionics Laboratory AFAL/DHO Wright-Patterson AFB, Ohio 45433		12. REPORT DATE May 1979
		13. NUMBER OF PAGES 66
14. MONITORING AGENCY NAME & ADDRESS(if different from Controlling Office)		15. SECURITY CLASS. (of this report) Unclassified
		15a. DECLASSIFICATION/DOWNGRADING SCHEDULE

16. DISTRIBUTION STATEMENT (of this Report)

Approved for public release; distribution unlimited.

17. DISTRIBUTION STATEMENT (of the abstract entered in Block 20, if different from Report)

18. SUPPLEMENTARY NOTES

19. KEY WORDS (Continue on reverse side if necessary and identify by block number)

Ladars
Optical Radar
Magneto-Optic laser beam steering
Bismuth Substituted rare earth iron garnets

20. ABSTRACT (Continue on reverse side if necessary and identify by block number)

The objective of this program was to provide mathematical analysis for the use of laser beam deflection in various potential applications. The analysis considered the effects of beam divergence, pointing accuracy, and signal-to-background noise. The analysis was supported by experimental measurements of relevant factors involved in the laser deflection process.

FOREWORD

This report was prepared by Sperry Univac, Applied Physics Laboratory, Univac Park, St. Paul, Minnesota, under Project Number 40179, Contract Number F33615-77-C-1163. The work was administered by the Air Force Avionics Laboratory, with Mr. Leslie J. Lawrence, AFAL/DHO as Project Administrator.

This summary report covers research conducted from July 1977 to August 1978 in the Applied Physics Laboratory, S. J. Lins, Manager. Members of the laboratory personnel who participated are: T. R. Johansen, E. J. Torok, J. A. Krawczak, F. G. Hewitt, G. L. Nelson, E. W. Simon, and W. A. Harvey. The report is submitted by the authors in October 1978.

iii

TABLE OF CONTENTS

LIST OF ILLUSTRATIONS

LIST OF ILLUSTRATIONS (continued)

LIST OF TABLES

SECTION I

INTRODUCTION

The major progress under the previous contract, contract number
F33615-75-C-1099, was development of the ability to grow crack-free
Bismuth-substituted rare-earth iron garnet films by liquid phase epitaxy.
This progress was made possible by the development of two-dimension x-ray
diffraction analysis capable of measuring in-plane lattice differences as
well as normal lattice differences.

Under the present contract major progress was made in several areas.
One of these areas is crystal measurements and evaluation. Included in
this area is the development of a useful method of measuring optical
absorption and the development of a computer-controlled crystal calibration
system for measuring pointing accuracy and other characteristics. A second
area of major progress was in the area of systems analysis which is devel-
oping the capability of specifying deflector properties for various appli-
cations. A third area of major progress that occurred during the contract
period was the growth of low-absorption films by means of calcium doping.

SECTION II

OPTICAL ABSORPTION MEASUREMENTS

A. Introduction

The problems in measuring optical absorption were a major obstacle in the development of high quality garnet films. The progress achieved in this area during this contract allows absorption measurements with sufficient accuracy for evaluation of experimental film development.

At the end of the previous contract period the error in measuring optical absorption was in the range of ± 200 db/cm. This estimate is based on the fact that calculated absorption coefficients were frequently negative. The optical absorption calculations were based on transmission coefficients measured on a spectrophotometer, refractive index measured by the Brewster's angle method at discrete wavelengths, and thickness from IR fringe spacing as measured on a spectrophotometer. The transmission measurement suffered from instrumentation errors which were not even known to exist at the time. The Brewster's angle measurements were subject to errors due to multireflections in the films. The fringe-spacing thickness measurements suffered from an estimated refractive index extrapolated from poor data in the visible.

During the interim period between contracts, the optical absorption problem was studied under a Univac IR&D program. Several methods of measuring optical absorption were considered. The method selected for development was a spectrophotometer measurement of the transmission coefficient (T), the reflection coefficient (R), and the interference fringe spacing ($\Delta\lambda$). To obtain the refractive index (n), the absorption coefficients (α), and the film thickness (t) combinations of n and k were tested in a programmed calculation until the measured values of T and R were obtained. A reflection attachment was fabricated for the Beckman DK2A spectrophotometer to facilitate reflection measurements.

2

The initial effort in this technique had a number of problems. The lack of a reference mirror was serious since the technique only compared the reflections of surfaces. In addition, errors due to absorptions and multiple reflection from two quartz-prism deflectors were difficult to over-overcome. In the data calculation, the n, α combination search was done manually and was very time consuming.

B. Progress

The preliminary results from the T, R, Δλ technique were sufficiently encouraging so that, when the present contract work started, the T, R, Δλ method was selected for further development.

1. Reflection Fixture

A new reflection fixture was made for the Beckman DK2A spectrophoto-meter and is shown in Figure 1. This fixture is interchangeable with the fixture used to measure liquid samples. In this picture the fixture is configured for the transmission measurement. The film sample is attached to the exit aperture of the fixture with double sided tape. The reference mirror is mounted on top in the reflection position. Two front surface mirrors near the center of the fixture deflect the beam to the reflection aperture. The sample is removed to make the reference curve measurement. The sample replaces the reference mirror for the reflection measurement.

2. Mirror Calibration Fixture

A calibrated reference mirror is required for the reflection fixture. A decision was made to develop an in-house mirror calibration capability. The fixture designed for this purpose is shown in Figure 2. The fixture holds four mirrors which deflect the light beam in a double "Z" path. The angle of incidence is approximately 7.5°. The mirror calibration fixture is used to measure the average reflection coefficient of four mirrors. The reflections of the individual mirrors are compared using the reflection fixture to obtain the reflection spectrum of an individual mirror.

3
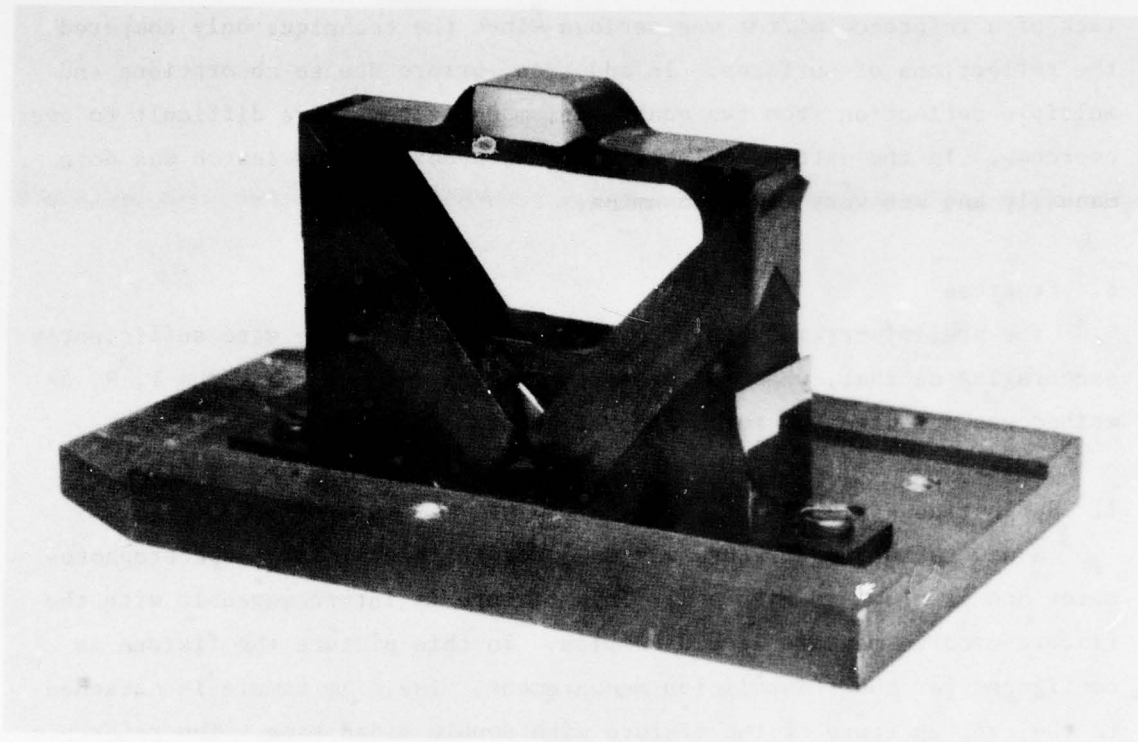
Figure 1.   New Reflection Fixture for the Beckman DK2A Spectrophotometer
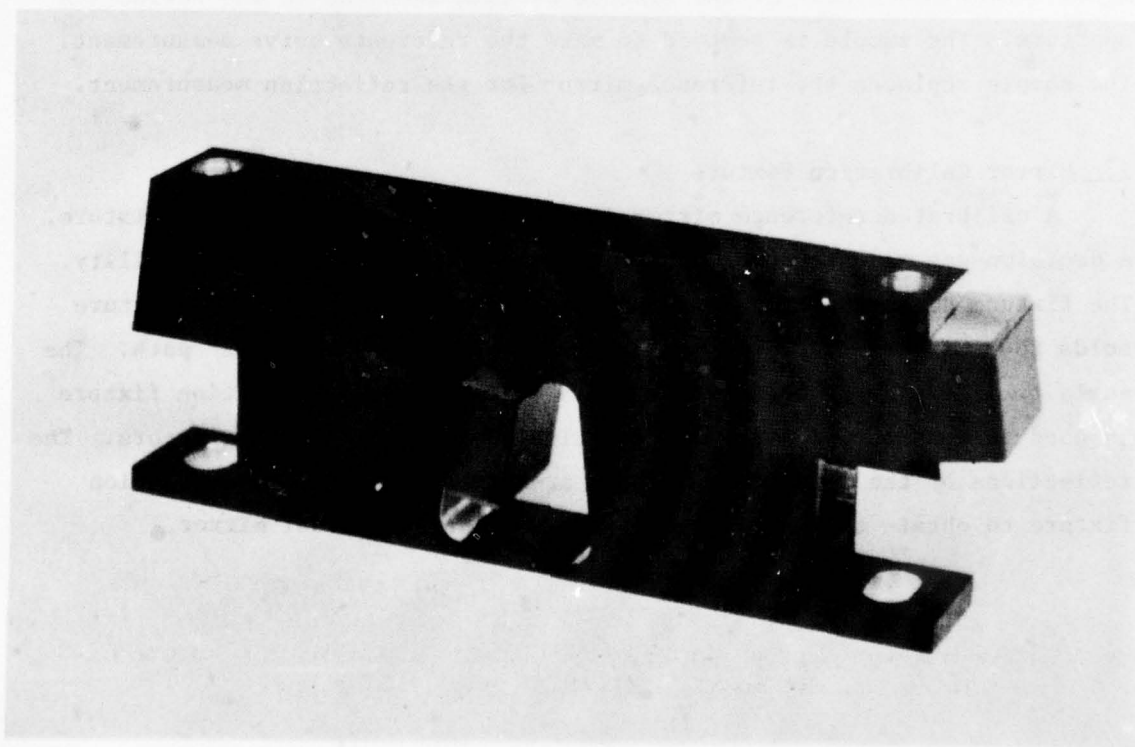
Figure 2.   Mirror Calibration Fixture

4

3. Substrate Transmission - Reflection Measurements

The new reflection fixture was first used to measure substrates. This
was done because the gadolinium gallium garnet substrates have known opti-
cal characteristics which could be used to check system calibration. In
addition, it was anticipated that information on substrate quality would be
obtained. The results of measurements on a large number of substrates was
very disturbing. There were large differences between substrates with many
substrates having combinations of transmission and reflection exceeding
100%. It became imperative to find the cause of these large errors.

Concurrent measurements were being made on the substrates for stress
birefringence and parallelism of faces. It was found that there was strong
correlation between the transmission-reflection measurements and the
parallelism measurements. Prompted by this correlation, an experiment was
conducted on two substrates in which the substrate was measured in several
orientations rotated about an axis normal to the film. The transmission
and reflection varied in a regular manner with the average value corres-
ponding with the expected published values. One remedy to this error is to
use substrate with very parallel faces. Another solution would be to use a
spectrophotometer with reduced sensitivity to small beam deflections.

4. Substrate Reference Technique

Two experimental methods have been developed for compensating the
parallelism error. In one method the substrate transmission-reflection
curves are measured before the film is grown. The ratios between the mea-
sured and expected coefficients are then used as correction factors for the
data taken on the subsequently grown films. Care must be taken so that the
same orientation is used for both sets of measurements. The orientation
error is one of several problems with this technique. A second problem is
instrument drift and instrument configuration changes that can occur during
the time between measurements when the film is being grown. Another

problem is the excessive substrate handling which is incompatible with the clean surface requirements for growth of high quality, low-defect films. Therefore, this technique was discontinued.

5.   In-Plane Angle Averaging Technique

The technique which is presently in use is similar to the substrate measurement used to verify the parallelism error. Transmission-reflection measurements are made every 45° for a total of 8 sets of data. Approximately one day is required for these measurements. In the substrate measurements each set of data was analyzed and then the results were averaged. This required approximately one week's time of data-reduction and calculation. In order to reduce this time requirement, transmission-reflection coefficients are examined at three wavelengths (1.0, 1.5 and 2.0μm) and the transmission and reflection curves which come closest to the average are then compensated to this average and used in the data reduction. This reduces data-reduction and calculation time to about one day. The error using this technique is estimated to be about ± 20 db/cm.

The development of this absorption measurement technique was a major accomplishment of this program. Without a suitable absorption measurement, it would be impossible to evaluate experimental techniques in the development of high quality garnet films. An example of this importance can be seen in a doping experiment in which a series of bismuth lutetium iron garnet films were grown with calcium added in increments of 5% of the lutetium component of the melt. Using the new absorption measurement techniques, calcium doping was shown to have significant effects on optical properties. Figure 3 shows the absorption coefficient at a wavelength of 1.06μm as a function of melt calcium content. The results show that a calcium content of 10% dramatically improves the optical transmission at 1.06μm by about a factor of 5 better than any previously grown film.
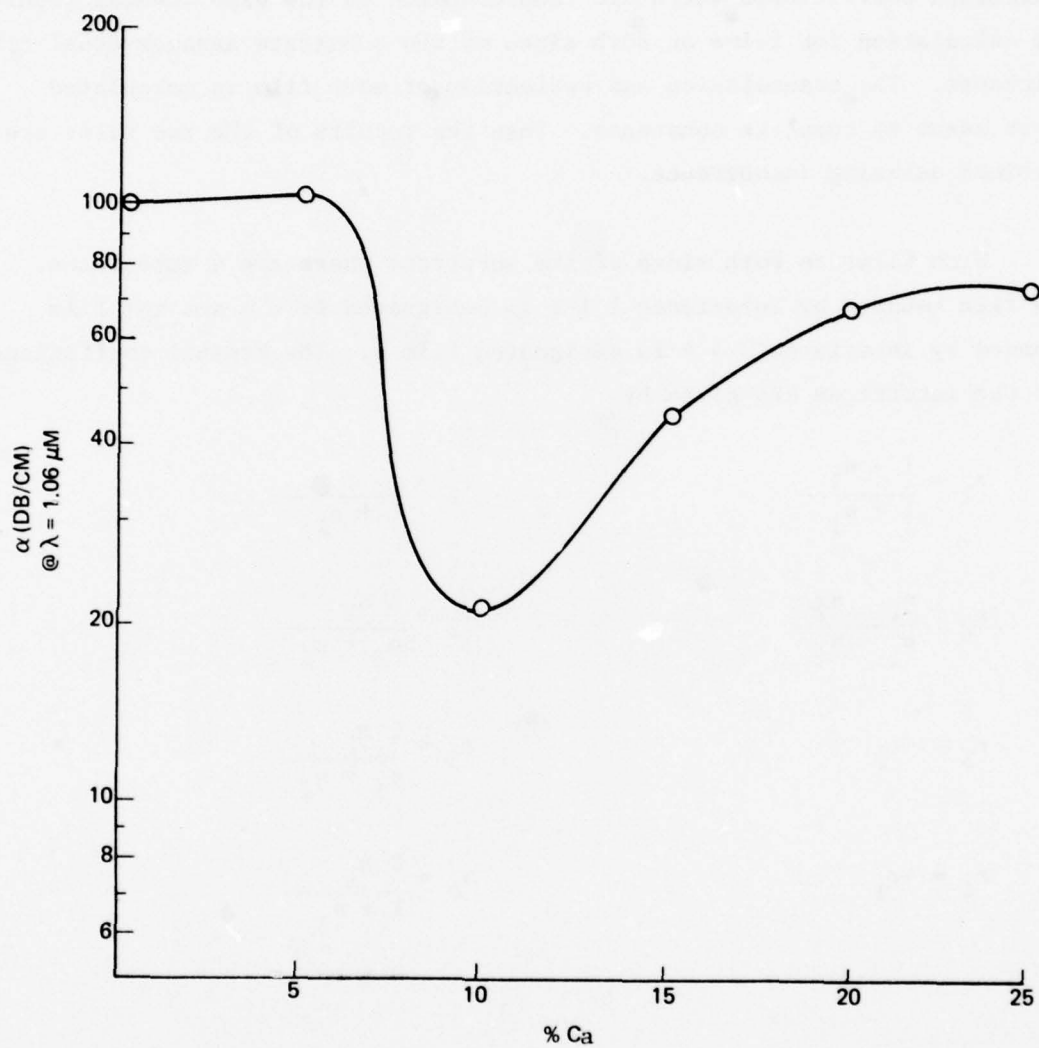
Figure 3. Absorption Coefficient at 1.06μm as a Function of Melt Calcium Content

6. Optical Calculations

The transmission, reflection, and fringe spacing data from the spectrophotometer measurements are used to calculate the refractive index, the absorption coefficient, and the film thickness. The calculation cannot be done in a straight forward manner. A combination of refractive index and absorption coefficient are used to calculate the transmission and reflection coefficients which are then compared to the experimental results. The calculation for films on both sides of the substrate assumes equal film thickness. The transmission and reflection of each film is calculated first assuming complete coherence. Then the results of the two films are combined assuming incoherence.

With films on both sides of the substrate there are 4 interfaces. The film bounded by interfaces 1 & 2 is designated film a and the film bounded by interfaces 3 & 4 is designated film b. The Fresnel coefficients for the interfaces are given by

$$r_1 = \frac{1 - n_1}{1 + n_1} \qquad\qquad t_1 = \frac{2}{1 + n_1}$$

$$r_2 = \frac{n_1 - n_2}{n_1 + n_2} \qquad\qquad t_2 = \frac{2\,n_1}{n_1 + n_2}$$

$$r_3 = -r_2 \qquad\qquad t_3 = \frac{2\,n_2}{n_1 + n_2}$$

$$r_4 = -r_1 \qquad\qquad t_4 = \frac{2\,n_1}{1 + n_1}$$

8

where n_1 and n_2 are the complex refractive index of the film and substrate and are given by

$$n_1 = n_1 - ik_1$$
$$n_2 = n_2 - ik_2$$

Combining the reflected and transmitted waves for film a by coherent addition to obtain the amplitude of the reflected and transmitted waves we have:

$$R_a = \frac{r_1 (\cos \delta + i \sin \delta) + r_2 (r_1^2 - t_1 t_4) (\cos \delta - i \sin \delta)}{(\cos \delta + i \sin \delta) + r_1 r_2 (\cos \delta - i \sin \delta)}$$

$$T_a = \frac{t_1 t_2}{(\cos \delta + i \sin \delta) + r_1 r_2 (\cos \delta - i \sin \delta)}$$

And similarly for film b

$$R_b = \frac{-r_2 (\cos \delta + i \sin \delta) - r_1 (r_2^2 - t_2 t_3) (\cos \delta - i \sin \delta)}{(\cos \delta + i \sin \delta) + r_1 r_2 (\cos \delta - i \sin \delta)}$$

$$T_b = \frac{t_3 t_4}{(\cos \delta + i \sin \delta) + r_1 r_2 (\cos \delta - i \sin \delta)}$$

where $\delta = 2\pi d_1 n_1 / \lambda$

and where d_1 is the film thickness and λ is the wavelength. The film thickness is an unknown but is related to the refractive index n_1 by

$$d_1 = \frac{\lambda^2 - (\Delta\lambda/2)^2}{2 n_1 \quad \Delta\lambda}$$

where $\Delta\lambda$ is the interference fringe spacing. The energy reflection and transmission coefficients are obtained by multiplying the amplitude by the complex conjugate and adjusting for the change in the refractive index. The reflection and transmission coefficients for the two films are therefore given by

$$R_a = \mathcal{R}_a \, \mathcal{R}_a^{*} \qquad\qquad T_a = n_2 \, \mathcal{T}_a \, \mathcal{T}_a^{*}$$

$$R_b = \mathcal{R}_b \, \mathcal{R}_b^{*} \qquad\qquad T_b = \frac{1}{n_2} \, \mathcal{T}_b \, \mathcal{T}_b^{*}$$

The reflection and transmission coefficients of the two films are added incoherently to obtain the final reflection and transmission coefficients

$$R = R_a + \frac{T_a \, T_b \, R_b \, e^{-2\pi k_2 d_2/\lambda}}{1 - R_b^2 \, e^{-4\pi k_2 d_2/\lambda}}$$

$$T = \frac{T_a \, T_b \, e^{-2\pi k_2 d_2/\lambda}}{1 - R_b^2 \, e^{-4\pi k_2 d_2/\lambda}}$$

where d_2 is the substrate thickness and k_2 is the substrate extinction coefficient.

A computer program to determine film refractive index, film absorption, and film thickness operates by searching for the combination of refractive index and absorption coefficient which results in the experimentally determined crystal transmission and absorption coefficients. The computer program is diagrammed in Figure 4. The inputs for the calculation are wavelength, interference fringe spacing, substrate refractive index, substrate extinction coefficient, substrate thickness, estimated film refractive index, and estimated film extinction coefficient.
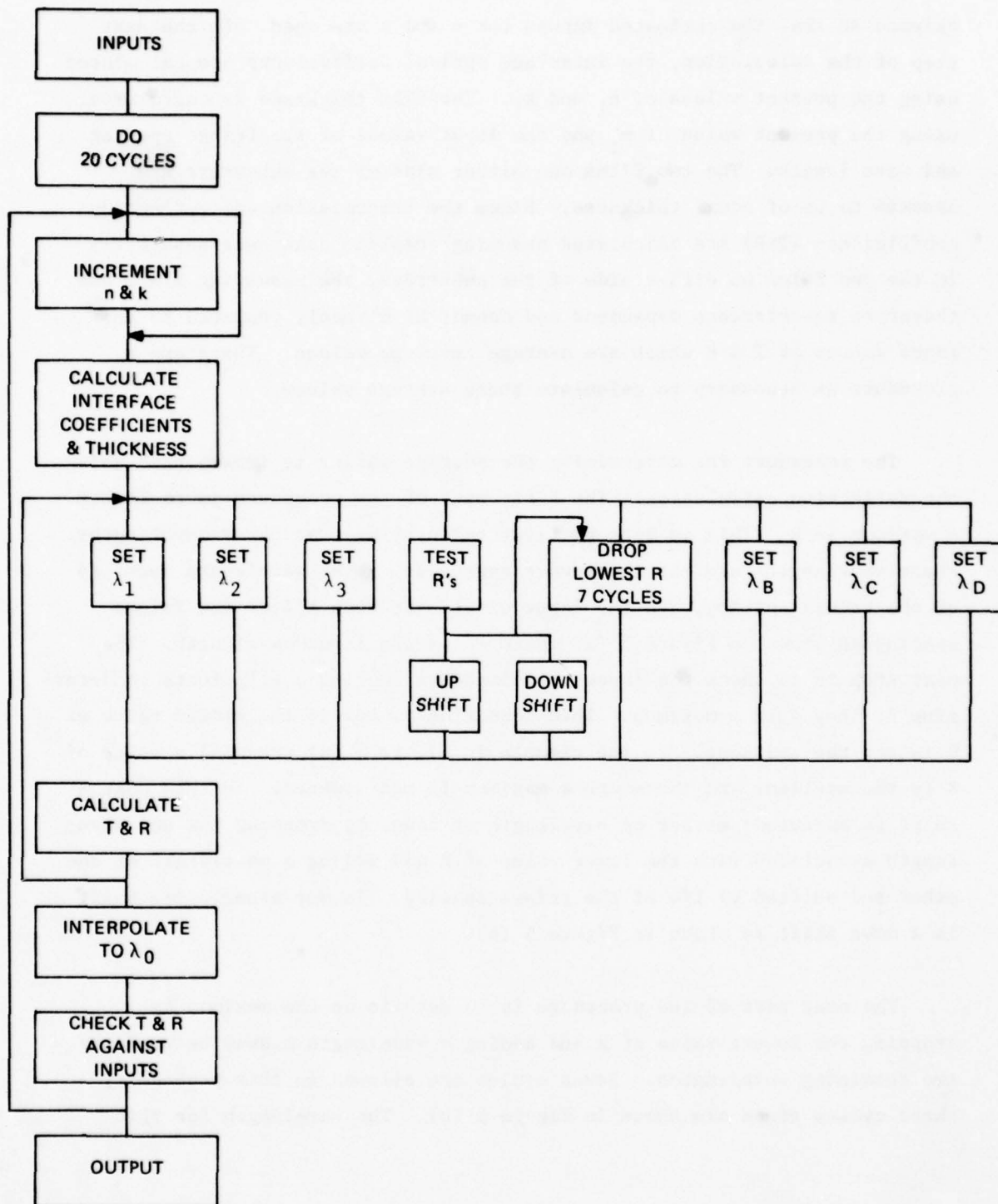
Figure 4. Computer Program to Determine Film Refractive Index,
Film Absorption and Film Thickness

11

In the first cycle through the calculations the increment step is skipped so that the estimated inputs for n and k are used. In the next step of the calculation, the interface optical coefficients are calculated using the present values of n_1 and k_1. The film thickness is calculated using the present value of n_1 and the input values of the fringe spacing and wave length. The two films one either side of the substrate are assumed to be of equal thickness. Since the transmission and reflection coefficients (T&R) are calculated assuming complete coherence separately in the two films on either side of the substrate, the resulting T & R are therefore interference dependent and cannot be directly compared to the input values of T & R which are average envelope values. Therefore a procedure is necessary to calculate these average values.

The procedure for determining the average values is implemented using the reflection calculation. The first part of the procedure is to locate a maximum in R. This is done by first calculating R at three wavelengths. These wavelengths are the input wavelength, the input wavelength less 1/4 of the fringe spacing, and the input wavelength plus 1/4 of the fringe spacing as shown in Figure 5 (a) where λ_o is the input wavelength. The next step is to check the three associated reflection coefficients to determine if they span a maximum. This condition is met if the middle value of R is not the smallest. In the example in Figure 5 (a) the middle value of R is the smallest and therefore a maximum is not spanned. In this case a shift is executed; either up wavelength or down, by dropping the end wavelength associated with the lower value of R and adding a wavelength at the other end shifted by 1/4 of the fringe spacing. In our example the shift is a down shift as shown in Figure 5 (b).

The next part of the procedure is to zero in on the maximum by dropping the lowest value of R and adding a wavelength midway between the two remaining wavelengths. Seven cycles are allowed in this procedure; three cycles steps are shown in Figure 5 (b). The wavelength for this

12

resulting maximum in R is labeled λ_A in Figure 5 (c). The wavelength for the next maximum in R and the next two minimums in R are calculated by decreasing the number of wavelengths in the film by increments of 1/4 waves. The resulting wavelengths (λ_B, λ_C, λ_D) and the corresponding values of R are shown in Figure 5 (c).

These resulting values of R are used in a linear interpolation (or extrapolation) to obtain the envelope values at λ_o as shown in Figure 5 (c). The average of the envelope values of both R and T are compared to the input values of R and T. If both coefficients are within the specified error limits (presently set at ± 0.0001) the calculation is terminated. If not n_1 and k_1 are incremented and the calculation is repeated as shown in Figure 4.

The value of k_1 is incremented on every cycle after the original cycle. The direction of the k_1 increment is determined by combining R and T to find the total energy loss. The value of k_1 is increased to increase the total energy loss and decreased to decrease the total energy loss. The magnitude of the initial increment for k_1 is 0.0001. When the k_1 increment is required to change sign its magnitude is decreased by a factor of 5.

The refractive index (n_1) is incremented only if one of the coefficients (R and T) is too large and the other coefficient is too small. The direction of the increment is determined from R. If the calculated value of R is too small, n is increased. The initial increment for n_1 is 0.01 and as with k_1, when the increment is required to change sign its magnitude is decreased by a factor of 5. At present a total of 20 cycles is allowed for the n_1, k_1 search. In this process 260 to 280 sets of R and T are calculated. If the calculation has not converged in 20 cycles, a new set of n_1, k_1 estimates can be entered and the calculation repeated.
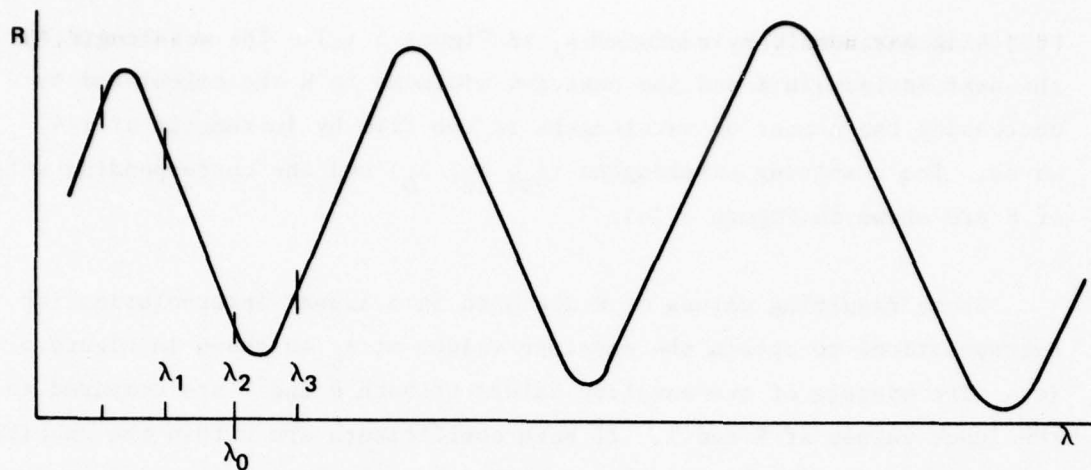
Figure 5(a).   R Calculated at Three Wavelengths
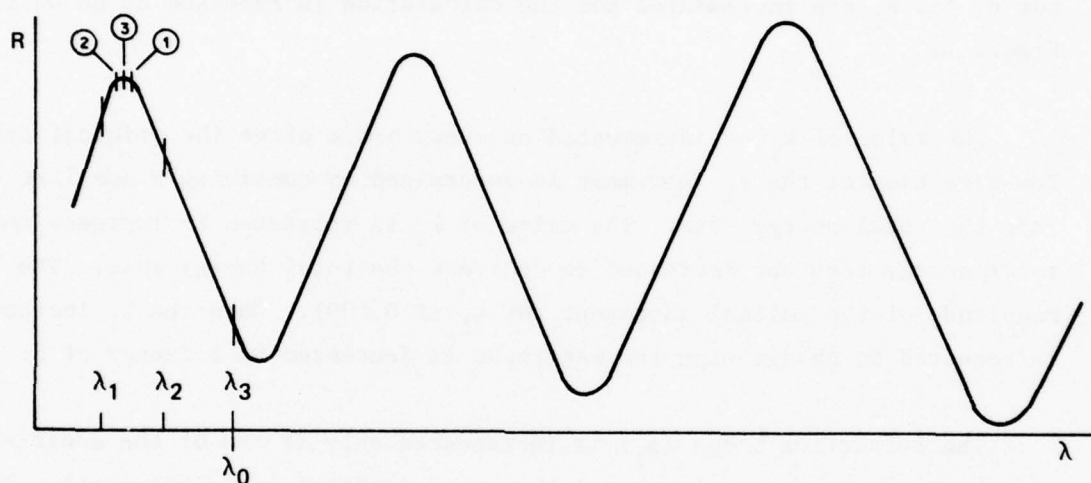
Figure 5(b).   Lowest Value of R Dropped; Wavelength Added (3 Cycle Steps)
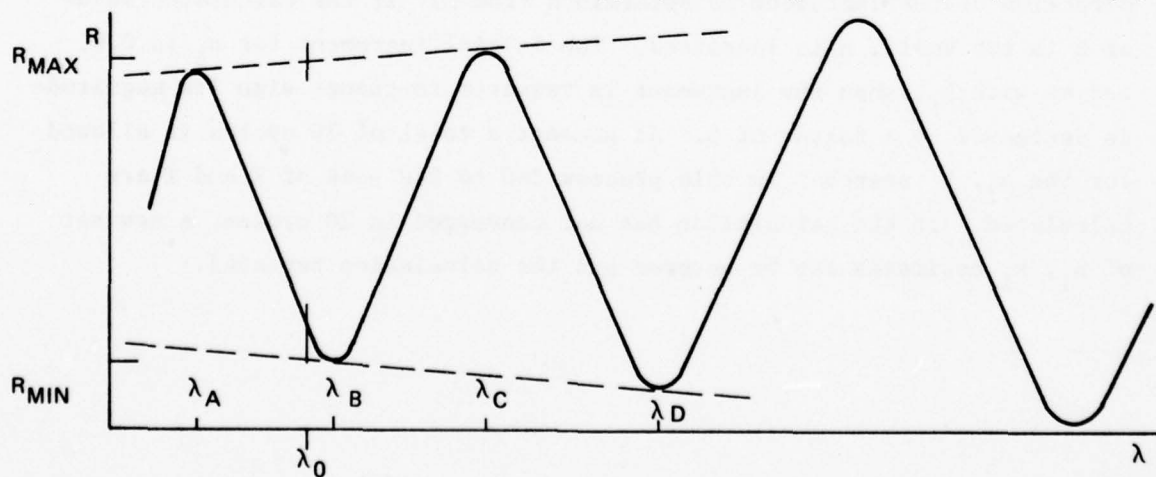
Figure 5(c).   Number of Wavelengths in the Film Decreased
by Increments of 1/4 Waves

14

In addition to giving a value for the reflection and transmission coefficients, the calculation also gives a value for film thickness as a function of wavelength. Since film thickness is independent of wavelength, its consistency is a check on the validity of the experimental data and calculation technique. After a first set of calculations the calculations are repeated using a fixed value for film thickness obtained by averaging the original results over a range of wavelengths.

At the beginning of the contract period the iteration of refractive index and absorption was done manually and was very time consuming. An iteration process has been programmed into the calculation resulting in considerable savings in calculation time. The iteration process has limits of $\pm$ .0001 on the transmission and reflection coefficients. The calculation converges rapidly and usually within 20 cycles which is an arbitrary limit used in the program. The time presently required for data reduction from the spectrophotometer plots and computer calculations is approximately one day.

7. Fringe Spacing Modulation

Spectrophotometer curves frequently exhibit amplitude modulation of the interference fringes. The probable source of this modulation is difference in the two film thicknesses. Attempts to incorporate this variable into the calculation have thus far been unsuccessful because it appears that the relation between the modulation and film thickness differences is very complex. However, it appears that the transmission and reflection are not strongly dependent on small thickness differences so that neglecting this modulation will not introduce significant errors.

8. Diffraction and Scattering

Optical measurements were made on a film to establish losses due to diffraction and scattering. Diffraction measurements were made at $1.06\mu m$ and extrapolated to other wavelengths. The first order diffraction loss

15

at 1.06μm was measured to be 0.0015 which reduces the calculated absorption factor of 150 db/cm by 4 db/cm. At .75μm the absorption coefficient was 285 db/cm and the extrapolated diffraction loss reduction is 41 db/cm. At 1.0μm the absorption coefficient was 50 db/cm and the extrapolated diffraction loss reduction is 1 db/cm. For this film, which is fairly typical, the diffraction loss correction does not appear to significantly effect the calculated absorption coefficient.

Scattering losses on the same film were estimated by using pit density distribution count from scanning electron micrographs and an estimated range of scattering cross sections. This particular film was moderately pitted and does not represent typical high surface quality films. The estimated correction ranged from 2 to 14 db/cm and was relatively independent of wavelength. It is therefore concluded that scattering losses do not appear to significantly affect the calculated absorption coefficient.

C. Conclusions

The development of an effective method of measuring optical absorption is one of the major accomplishments of the light deflector program. Without this measurement it would be extremely difficult to evaluate crystal growing techniques which would result in high-quality, high-efficiency light deflectors.

16

SECTION III

FILM MEASUREMENTS

A. Anisotropy

The triaxial crystalline anisotropy in garnet deflectors opposes attempts to rotate a stripe domain grating. Instead of rotating as a rigid unit the grating breaks up into short batches of stripes which tend to point along the preferential axes. In the past this has been countered by first erasing the stripes with a saturating in-plane field, rotating the magnetization in the plane as a single domain, and then, reinstating the stripes along the desired direction. Unfortunately, the rather large saturating fields require that drive currents be switched in short time intervals. This demands a considerable amount of power and band-width from the delivery electronics, and although electronic circuitry can be designed to be extremely flexible it is more important in the long run to seek an understanding of the grating limitations at the crystal level. With this in mind a company sponsored IR&D program was launched for the purpose of investigating the physics of the triaxial in-plane anisotropy. Both theoretical and experimental avenues are to be pursued in an attempt to understand and ultimately control this anisotropy.

The first step in the experimental direction was the design and construction of a magneto-optic hysteresigraph, capable of pinpointing the value of the anisotropy field at any direction in the plane of the film. Figure 6 is a block diagram of the apparatus. Polarized visible light that passes through the crystal is captured by the microscope, is optically analyzed, and then is brought to convergence in the focal plane of a photodiode. The photodiode signal is amplified and then taken to the numerator input of a precision analog divider. Denominator information is acquired from a second photodiode that monitors the instantaneous intensity of the light source. This mathematical processing insures that low level magneto-optic signals are not masked by fluctuations in the light source.

Two magnetic fields are present in the sample plane. A large field along the optic axis of the assembly provides for saturation normal to the sample while a smaller field is used for in-plane saturation. The sample can be rotated 360° about the optic axis so that in-plane fields can be placed along any direction in the sample. Calibration constants transfer the field magnitudes to the display. In this way continuous recording of the data is possible.

Figure 7 is a photograph of the magneto-optic hysteresigraph apparatus.

B. Stress Birefringence and Parallelism Measurements

Stress and surface parallelism measurements were made on G^3 substrates to investigate their importance in growing high-quality garnet films. Many of the films which we polished in our laboratories showed patterns of residual stress. Sufficient data was not collected to determine the effects of these stresses. High quality substrates which were purchased later in the program did not exhibit stress birefringent patterns. Therefore, residual substrate stress is not deemed a serious problem.

Surface parallelism measurements on G^3 substrates led to the discovery of a serious error in the absorption measurements. The development of the absorption measurement to compensate for non parallelism has eliminated the requirement to make routine parallelism measurements on substrates. However, a high degree of parallelism might become advantageous for deflector crystals inserted into a laser cavity.
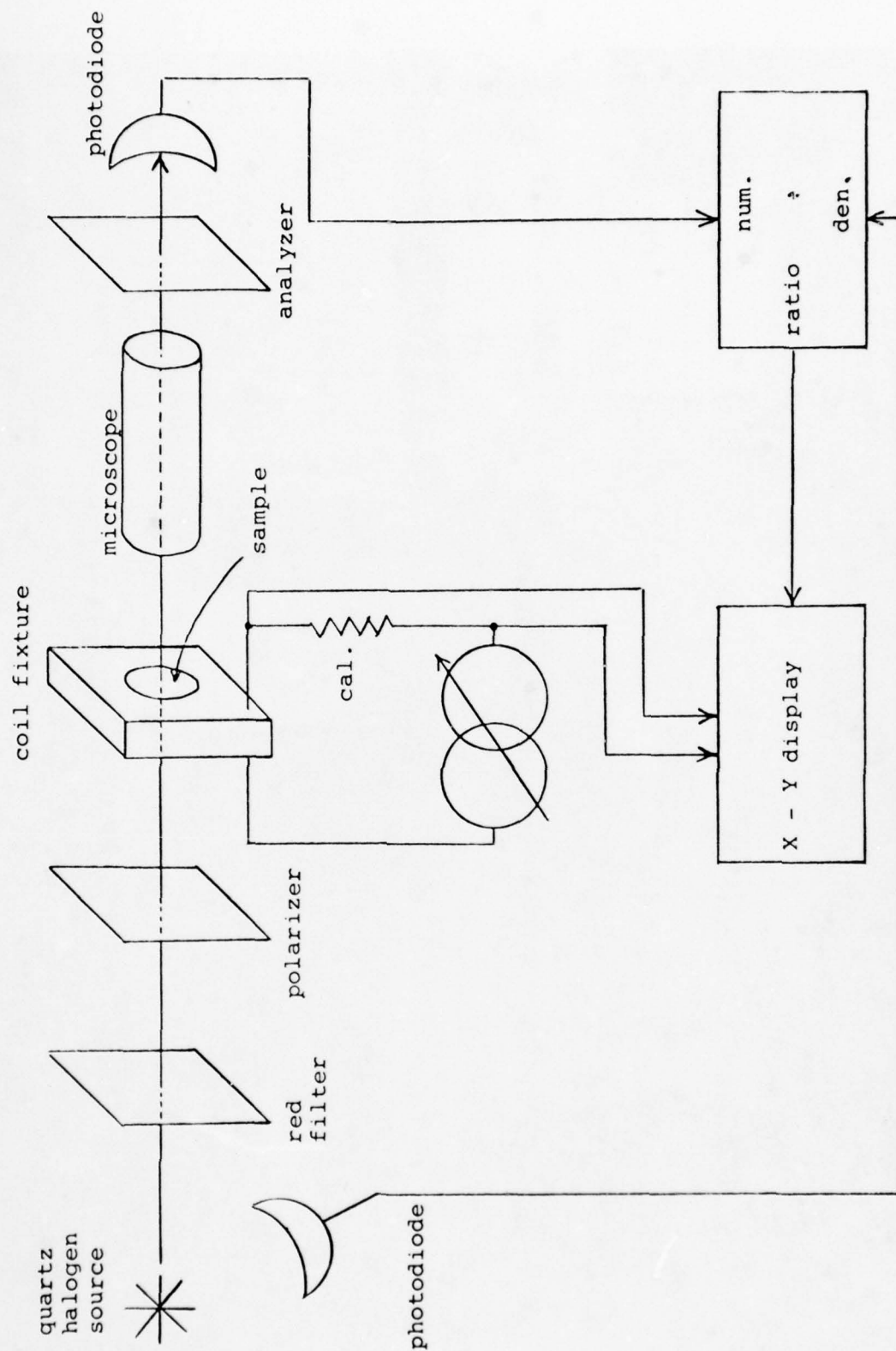
Figure 6. Block Diagram of the Magneto – Optic Hysteresigraph

19
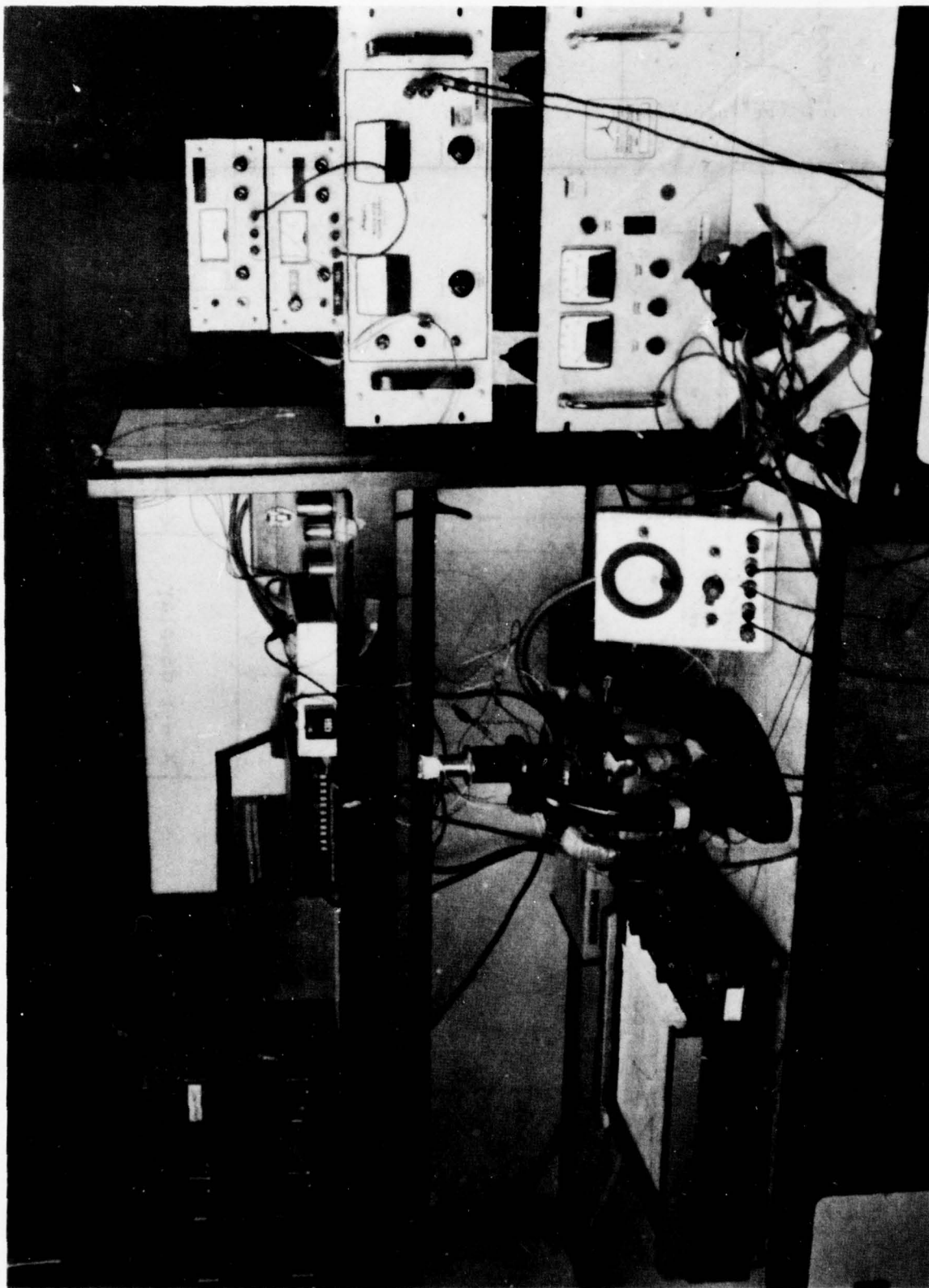
Figure 7. The Magneto - Optic Hysteresigraph

20

SECTION IV

FILM GROWTH AND FACILITIES

A. Introduction

Crystal production under this program was principally directed towards providing experimental samples necessary for the development and utilization of measurement techniques important in determining the present state of Bi-garnet light deflector production. All of the samples produced were bismuth-substituted lutetium iron garnet crystals grown from $PbO-Bi_2O_3$ fluxes. In the process of studying deflector crystals, while developing measurement capabilities and determining deflector performance limits, techniques or experiments which might provide materials development advancement became apparent. These avenues of improvement were incorporated into the sample production work whenever possible - i.e. the basic sample production work would not be interfered with or lengthened. The result is that deflector performance has been significantly improved in terms of both resolution and efficiency compared to the early contract period. Bi-garnet crystals grown prior to and in the early stages of this program were of high mechanical quality. Specifically, the crystals were uncracked, strain-free, epitaxial samples with excellent surface smoothness (naked eye) and good thickness uniformity. Deflector performance, however, was significantly degraded by thousands of defects per square centimeter and by high optical absorption.

B. Defect Problem

A first study involved determining defect types and densities and revealing defect causes. Initial Bi-Lu-Fe garnet crystals were grown in a medium purity 3-9's to 4-9's melt in an unfiltered environment on GGG substrates obtained from the Sperry Research Center (polished at Univac). This represented typical, if not identical, conditions for most previous deflector crystals produced (a few exceptions being grown in higher purity melts). A representative sample with the requisite high mechanical quality

21

was selected for detailed study. This crystal was etched in 180°C
phosphoric acid to reveal the defects for scanning electron microscope
photography. Photos 1, 2 and 3 were made after this strain selective
etching and a Au–Pd deposition to prevent charge build-up. The photos
show the three defect types located; 1) penetrating defects, 2) non-
penetrating defects and 3) clusters of penetrating defects. It is believed
that the penetrating type defect is generated by point defects in the
substrate and that the clusters of penetrating defects are generated by
substrate inclusion dislocations. The non-penetrating defect type is
associated with either environmental dirt or spontaneous nucleation at the
substrate surface or trapped as an inclusion when growing the epitaxial
layer.

C. Defect Reduction

Subsequent crystal sample production incorporates refinements which
improves or lower defect densities. The improvement is a direct result of
low defect-density substrates, careful cleaning procedures, high melt
purity, and an improved environment due to a laminar flow hood-furnace
system which was constructed.

Allied chemical low defect density substrates with less than 1 defect/
cm^2 are being cleaned in a class 100 facility. The cleaning procedure
specifically involves:

1) an acknowledgement rather than a repeat of the $H_3PO_2 + H_2SO_4$
   acid etch and cleaning performed by Allied.

2) removing accumulated dust or dirt by spinning the substrate at
   10,000 r.p.m. while spraying it with high-pressure deionized
   water.

22

PHOTO 1: Penetrating Defect
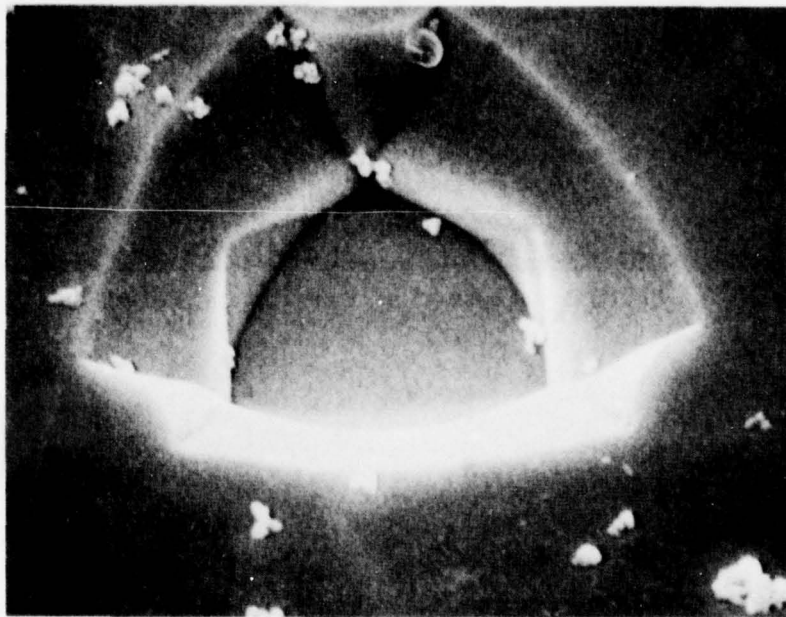
PHOTO 2: Non-penetrating Defect

23
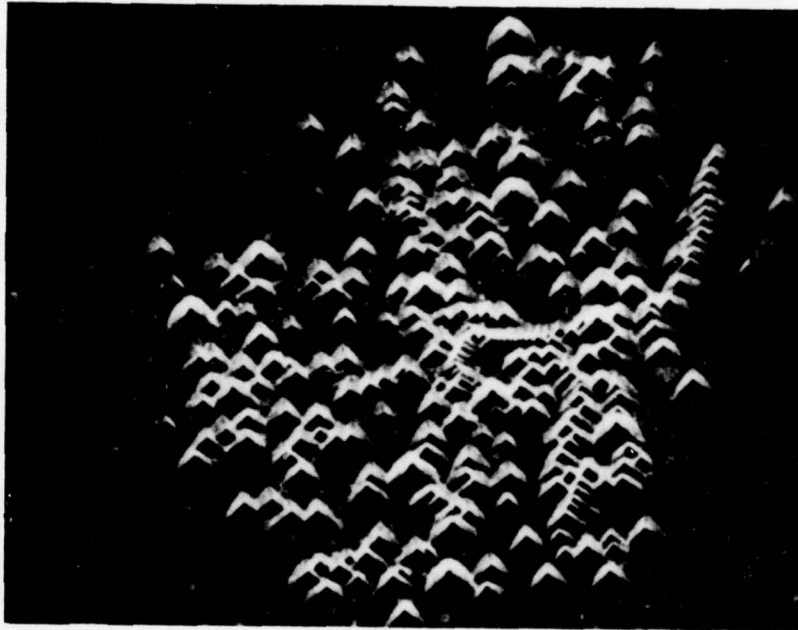
PHOTO 3: Cluster of Penetrating Defects

3) removing remaining deionized water by continuing to spin the substrate at 10,000 r.p.m. when the spray is stopped.

4) transferal of the clean substrate to the growth facility in a sealed and meticulously cleaned container.

Optical observations indicate that this procedure is effective and provides a much improved surface suitable for epitaxial growth.

Table 1 shows a typical high purity melt (6-9's) used as a means of reducing the number of defects.

Table 1

Compound	m moles	grams	mole percent
Bi_2O_3	708.30	330.06	25.57
PbO	179.0	400.00	64.70
Fe_2O_3	255.78	40.846	9.24
Lu_2O_3	13.650	5.396	.49

An improvement in starting purity has been found to extend the metastable region slightly. This extension reduces the level of spontaneous nucleation in the melt and thereby aids in preventing inclusion-type defects caused by entrapment of the nucleation. Additionally, high purity melts were desirable for the calcium-doping charge compensation growth experiments.

The laminar flow hood-furnace system allows the previous improvements to be implemented. High quality substrates and cleaning procedures provide minimal improvement in defect count if dirt cannot be effectively kept off the epi-surface. Room dust is also an effective and non-negligible means of melt contamination or uncontrolled melt doping - the laminar system reduces this.

The improvement in crystal quality is apparent in beam deflection observations. The best results indicate a beam divergence of 1-1.25m radians. Additionally, this performance can be obtained quite consistently as different areas of the crystal are used. The improvement implies, minimally, an increase in the number of resolvable spots by a factor of 5 over the best previously grown sample and a factor of 15 over typical previously grown samples.

D. Doping Experiments

With the successful development of an optical absorption measuring technique it became feasible to study the effects of doping in the bismuth lutetium iron garnet. A fresh, high-purity melt was constructed, characterized, and used to produce "control" samples. Using a representative sample, Corbino disc-modified Seebeck measurements were conducted to determine excess carrier type. This indicated "n" type behavior for crystals produced with the specific melt impurity concentrations present during the control production period. For a general melt, specific impurity concentrations depend on starting chemical impurities, environment contributed impurities with their respective time dependencies, dissolution with thermal cycling of the platinum crucible, and differential removal from growing or volitization activities. Based on the "n" type determination from the experimental melt, a series of crystals was produced with incremental additions of CaO to the melt. To minimize the environmental dissolution and drift effects, the series was produced as rapidly as possible with a minimum in melt high-temperature soaking. CaO was added in increments of 5% of the Lu_2O_3 present in the melt. An addition was made after each sample produced with the final cumulative addition reaching 50% of the Lu_2O_3. As discussed in the Optical Absorption section, this not only provided a definitive test sequence for the absorption measurement but resulted in significantly improved deflector crystals. Crystal number GLN286 included in Table 2 represents the best diffraction ever produced;

26

1.06 μm wavelength absorption of 21 db/cm, Faraday rotation of approximately 200°/μm, and beam divergence of approximately 1.2 milliradian

E. Mesas

Tapered-edge mesas were produced on three bismuth lutetium garnets. Several approximately one-millimeter apertures with no defects were formed. Defect-free regions of the sample were selected by observing the crystal in an optical microscope using an illuminating light beam smaller than the field of view. When an appropriate defect-free region of the crystal was observed in the illuminated area, the upper portion of the microscope was detached leaving the exposed defect-free region pin pointed by the light beam. It was then possible to accurately place the epoxy mask over the defect-free region. With the epoxy mask formed, ion-machining was used to remove surrounding crystal material leaving a tapered edge mesa.

After the mesas were formed, optical studies were undertaken. Initial observations were of beam deflection resolution comparing the mesa area to the original "complete" epitaxial layer. Surprisingly, the defect-free aperture, combined with the tapered edge to improve vertex domain behavior and domain nucleation, had poorer resolution than the original layer. To determine why, the domain patterns were observed. It was found that because of crystal edge-domain interactions the grating was distorted as exaggerated in Figure 8. To alleviate this distortion, two Mu-metal keeper structures were studied. The first structure was simply Mu-metal much thicker than the crystal mesa with a hole drilled in it of a diameter matching that of the mesa. This structure was placed around the mesa and the domains again viewed after magnetic fields were applied. This time the domains showed the opposite distortion as exaggerated in Figure 9. This was explained by the formation of magnetic poles at the keeper edge surrounding the mesa because of the thickness of the keeper. The resulting field would be perpendicular to the edge resulting in the observed grating distortion. A second keeper structure was constructed with a square hole,
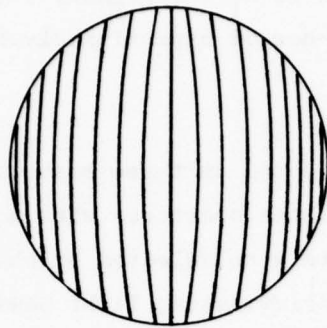
Figure 8. Distorted Grating
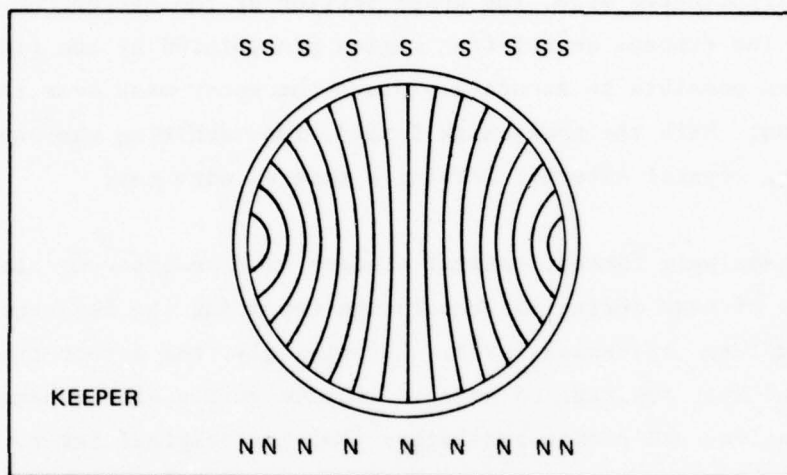
Figure 9. Domains Show Opposite Distortion
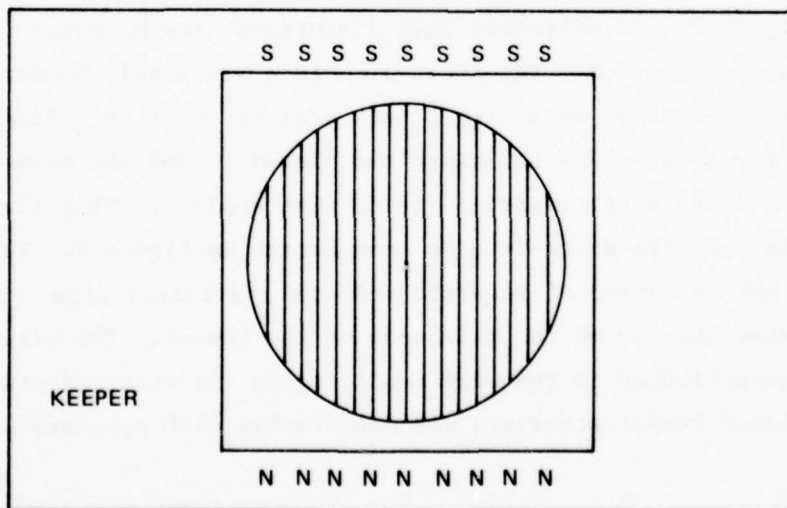
Figure 10. Second Keeper Structure with Square Hole

as in Figure 10. Repeating the observations showed that with the applied magnetic field normal to a pair of the squares' edges, a straight domain grating was formed. The explanation in this case is not as certain but believed to be dependent on the magnetic poles formed along the keeper and keeper thickness related to the mesa.

The observations performed in this section demonstrate that both edge effects and keeper structures can significantly affect grating uniformity. More detailed studies of these effects will be required when larger diameter defect-free apertures are available.

F. Crystal Production

Table 2 lists all of the crystals produced under this contract. The samples fall into four general categories. (I) GLN255 to BH002 are samples grown on high-defect density substrates without special cleaning procedures or a laminar hood environment. These samples were used primarily in studying the defect-type defect-source problem. (II) GLN273 to GLN284 are samples on both high and low-defect density substrates without the laminar hood environment. These samples were produced to aid in crystal mesa activities. (III) GLN285 to BH079 were grown primarily on low-defect density substrates with special cleaning procedures and utilizing the laminar hood furnace constructed during the contract period. These samples were produced to determine minimum beam divergences obtainable within the cost-time constraints of the program. (IV) BH084 to BH107 were produced with low-defect density substrates and cleaning procedures but without using the laminar hood furnace. This series of crystals was produced with the calcium doping for charge compensation study and utilization of the developed optical absorption measurement procedure.

G. Antireflection and Mirror Coatings

In the very early stages of the program a number of crystals had the films removed from one side of the substrate and antireflection and mirror

TABLE 2

CRYSTAL NUMBER	MELT NUMBER	Δa IN Å	Tg IN °C	tg IN MINUTES	THICKNESS IN μM	LOW DEFECT SUBSTRATE?	FURNACE	1.06μM ABSORPTION(db/cm)
GLN255	M175	0	737	21		NO	LARGE	
GLN260	M175HP	.017	723	10		NO	LARGE	
GLN261	M175HP	.009	721	5		NO	LARGE	
GLN262	M175HP	.010	721	7		NO	LARGE	
GLN263	M175HP	0	710	4		NO	LARGE	
GLN264	M175HP	*	721	4		NO	LARGE	
GLN265	M175HP	*	723	7		NO	LARGE	
GLN267	M175HP	*	715	7		NO	LARGE	
GLN268	M175HP	*	715	11		NO	LARGE	
GLN269	M175HP	.007	711	20		NO	LARGE	
GLN270	M175HP	*	710	22		NO	LARGE	
GLN271	M175HP	NM	710	20		NO	LARGE	
GLN272	M175HP	NM	710	20	7.7	NO	LARGE	137
BH001	M175HP	NM	738	20		NO	LARGE	
BH002	M175HP	NM	738	20	9.8	NO	LARGE	44
GLN273	M175G	0	699	8		NO	SMALL	
GLN274	M175G	0	706	9		NO	SMALL	
GLN275	M175G	.021	721	10		NO	SMALL	
GLN276	M175G	.018	709	15		NO	SMALL	
GLN277	M175G	0	715	5		NO	SMALL	
GLN278	M175G	0	715	21		YES	SMALL	
GLN281	M175G	*	718	10		YES	SMALL	
GLN283	M175G	NM	715	18		YES	SMALL	
GLN284	M175G	*	716	20		YES	SMALL	
GLN285	M193	.031	720	20		NO	LAMINAR	
BH065	M193	.006	684	15		NO	LAMINAR	
BH067	M193	0	690	14		NO	LAMINAR	
BH069	M193	.007	694	15		YES	LAMINAR	
BH071	M193	0	690	10		YES	LAMINAR	
BH075	M193	.007	689	12		YES	LAMINAR	
BH077	M193	NM	677	10		YES	LAMINAR	
BH079	M193	-.006	701	10		YES	LAMINAR	
BH084	M193	-.007	716	5		YES	LARGE	
BH087	M193	-.002	719	6		YES	LARGE	
BH089	M193	-.002	720	6	3.3	YES	LARGE	100
BH092	M193	NM	715	19	11.3	YES	LARGE	95
GLN285	M193	NM	721	20	19.1	YES	LARGE	
BH093	M193	NM	720	20	12.1	YES	LARGE	104
GLN286	M193	NM	723	23	11.1	YES	LARGE	21
BH095	M193	NM	721	20	12.2	YES	LARGE	45
BH096	M193	NM	720	20	11.7	YES	LARGE	68
BH098	M193	NM	275	20	12.0	YES	LARGE	70
BH100	M193	NM	721	20		YES	LARGE	
BH101	M193	NM	722	20		YES	LARGE	
BH103	M193	NM	725	20		YES	LARGE	
BH105	M193	NM	727	20		YES	LARGE	
BH107	M193	NM	717	20		YES	LARGE	

Table 2 List of Crystals Produced

* ~ Measurement was made but, because of growth temperature control problems,
    lattice mismatch is a continuum rather than a specific value.

NM ~ Not Measured: X-ray measurement frequently was not made if the 0 mismatch
    temperature had been determined for the specific melt within its recent
    operating past (i.e. volitization effects still minimized)

30

coatings applied. The antireflection material was SiO and the mirror material was aluminum. Both coatings were applied by vacuum deposition. Spectrophotometer measurements were made before and after the coatings were applied. These measurements indicated that these coatings were very effective in reducing first surface reflection and in providing a reflection device. However, at that time, the spectrophotometer measurement technique had not been fully developed and accurate calculation could not be made. Although additional coating experiments have not been made, no undue difficulties are expected in this area.

SECTION V

DEFLECTOR PERFORMANCE ANALYSIS

A. Deflector Characterization

The maturation of the crystal growth techniques has brought about the need for an examination of the garnet deflector as a system component. To this end apparatus were designed and constructed to allow for automatic determination of both the repeatability and the spatial resolvability of stripe domain garnet deflectors.

Figure 11 is a block diagram of the entire measurement console. It represents the merging of several rather independent technologies for the purpose of controlling and monitoring the location of a steerable laser. Current laser beam technology is utilized in conjunction with a stripe domain garnet crystal to realize solid state deflection. A conventional Univac UYK/20 computer provides digital commands for the crystal's magnetic drivers and also looks at the digitized version of the actual position of the laser beam. In the middle stands analog to digital and digital to analog electronic circuitry that interface the crystal with the computer.

The salient measurements made by this system include the two magnetic coil currents and either two or four signals that are derived from a four quadrant cartesian photodiode that is placed in the path of the deflected beam. With reference to Figure 11, the measurements are acquired by the following procedure. The UYK/20 computer selects from memory two 16 bit digital words that correspond to the Polar (R,θ) coordinates of a set of coil currents. A subroutine rapidly transforms these two words into digital cartesian coordinates representing first the calculated saturation field required to properly initialize the deflector grating and secondly the hold field required to momentarily aim the beam in a specific orientation. At this time there is enough information at the output channels of the computer
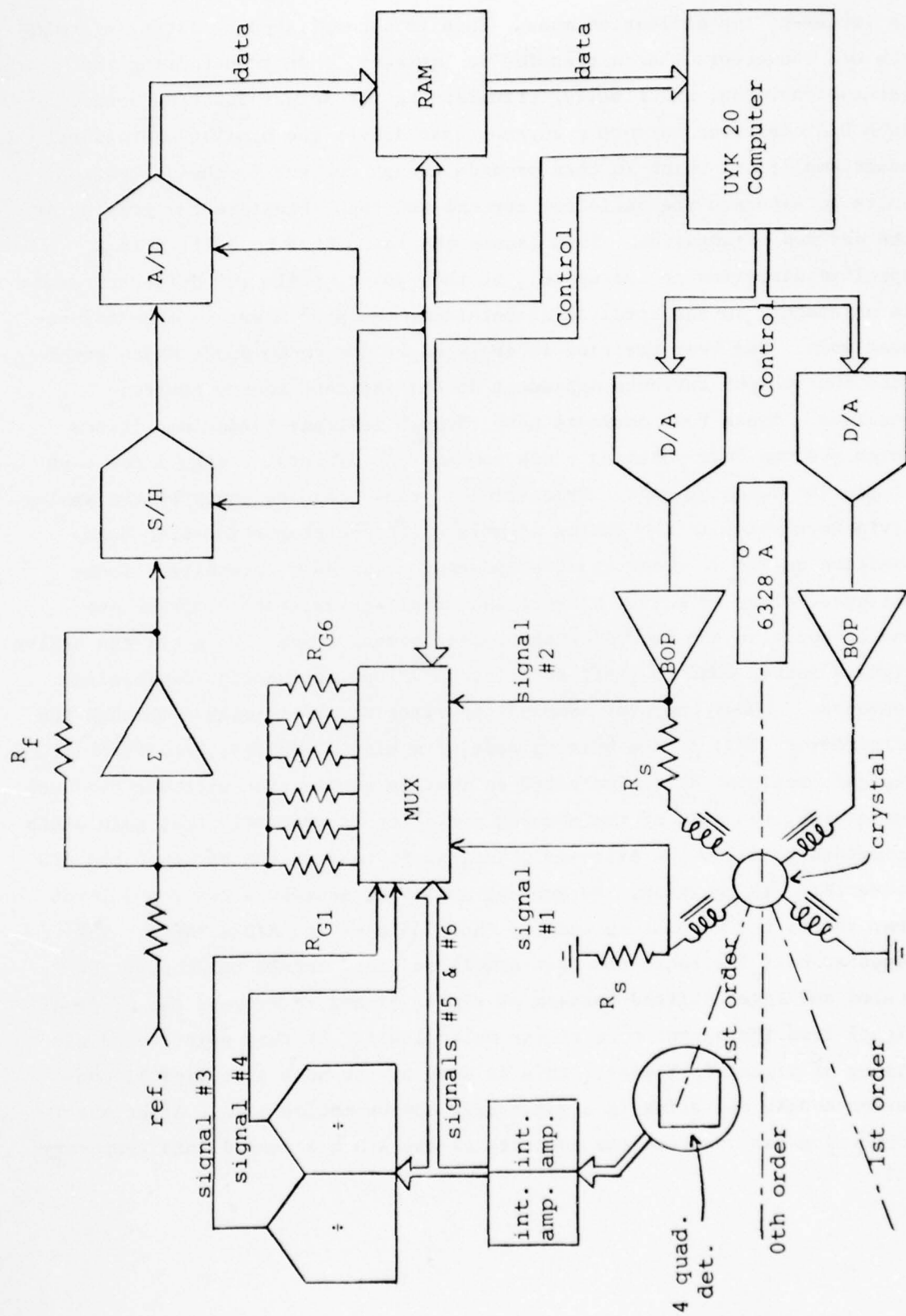
Figure 11. Block Diagram of Measurement Console

33

to implement the deflection mode. This is accomplished by first informing the D/A converters that a transfer is imminent, then transferring the saturation words, and finally, transferring the actual position words. Each D/A converter outputs a current that drives the bipolar operational power amplifiers which in turn provide enough current to the deflection coils to saturate the deflector crystal and then reinstate the grating at the desired orientation. This causes the laser beam to deflect in a specific direction in two space. At this point, while the deflected beam is maintained in the specific orientation, the system enters the measurement mode. The beam position is analyzed by the photo diode which generates four output currents dependent on the incident energy centroid position. These four currents pass through instrumentation amplifiers which produce four voltages - one sum and one difference signal for each of the two detector axes. Processing of these four voltages by the analog dividers results in two analog signals which are proportional to beam position on the detector and are independent of beam intensity. These voltages, along with the coil-current sampling resistors comprise one analog point in the four coordinate measurement space. Once all the analog signals settle down to their equilibrium values, sequential digitizing commences. Under computer command the first signal is passed through the multiplexer (MUX) to the summing node of a simple additive amplifier (Σ). The gain resistor R_{G1} is selected so that in combination with the feedback resistor R_f the gain of the summing amplifier is precisely that gain which is needed to allow the extremes of signal #1 to span the range of the A/D converter. In addition, the summing amplifier accepts a reference level that shifts the 0 point to exactly the middle of the A/D's range. The computer next instructs the fast sample and hold module to acquire the scaled and level shifted version of signal #1 and to release the original signal from the output port of the multiplexer. At this point the digitizing of signal #1 begins. This is done by the analog to digital converter module operating in a successive approximation mode. After the conversion has occurred the contents of the A/D are dumped into temporary

storage in the random access memory (RAM). In the same manner are processed the rest of the analog signals so that the RAM eventually holds the digitized representation of each variable for one point in measurement space. Finally, the RAM contents are transferred into the UYK/20 and the cycle is complete. Thus, in just a few milliseconds the salient information on the position of the laser beam is obtained.

Such a closed loop data tracker is a valuable asset for tabulating the dynamical characteristics of stripe domain deflectors. Once the computer has finished assembling the data necessary for evaluating the desired deflector performance characteristics it can call up its calculating power to make the evaluations and statistical reductions. Performance in critical areas like resolution, in-plane anistropy effects and repeatability are examples of important performance areas which can be studied. All of this information can then be stored in a computer file as a convenient, permanent record of the characteristics of one crystal. Subsequently the file can be recalled for comparisons with files of other crystals.

Presently the system is capable of selecting sixty-five thousand vector magnetic field values to orient the deflector. The pointing accuracy of a crystal can be measured to 256 x 256 points resolution after digitizing the photo diode position data. However, if less than the full field of view of the deflector is studied, the 256 x 256 resolution can correspond to arbitrarily small deflection beam movements. If this becomes a limitation, the system can be conveniently expanded to 1000 x 1000 resolution points.

Figure 12 is a photograph of the deflector characterization test system. Figure 13 is a close-up photograph of the light deflector and detector. Figure 14 is a photograph of the four quadrant cartesian photodiode.
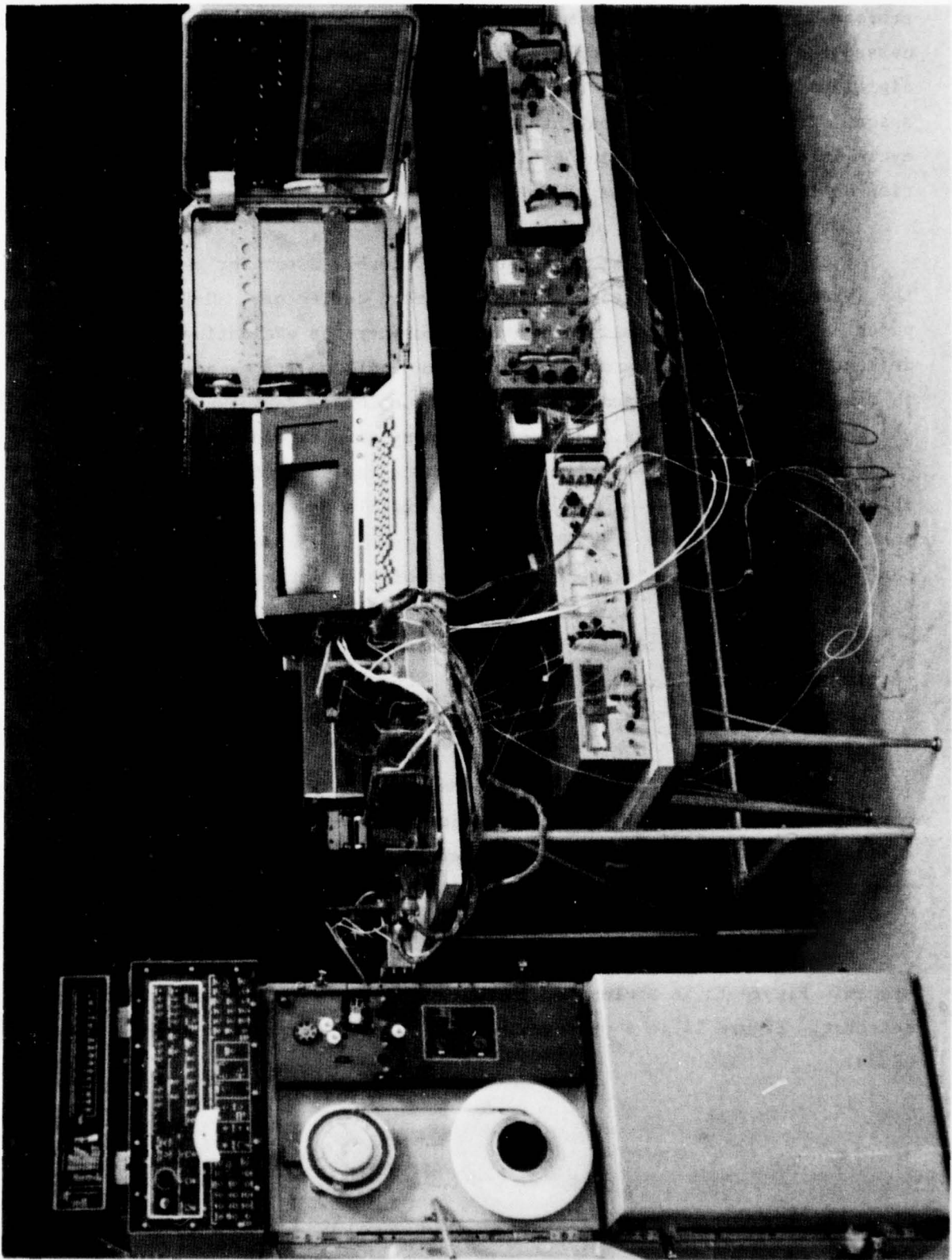
Figure 12. Deflector Characterization Test System
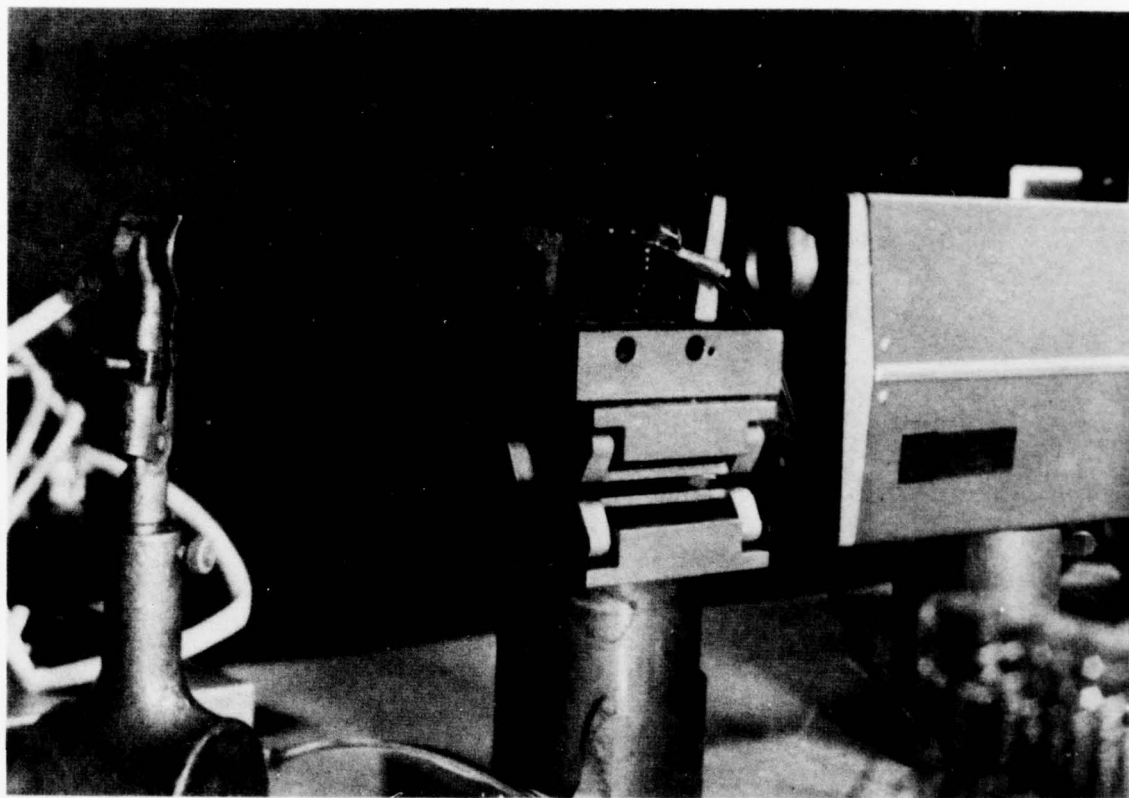
Figure 13. Close-Up of Light Deflector and Detector
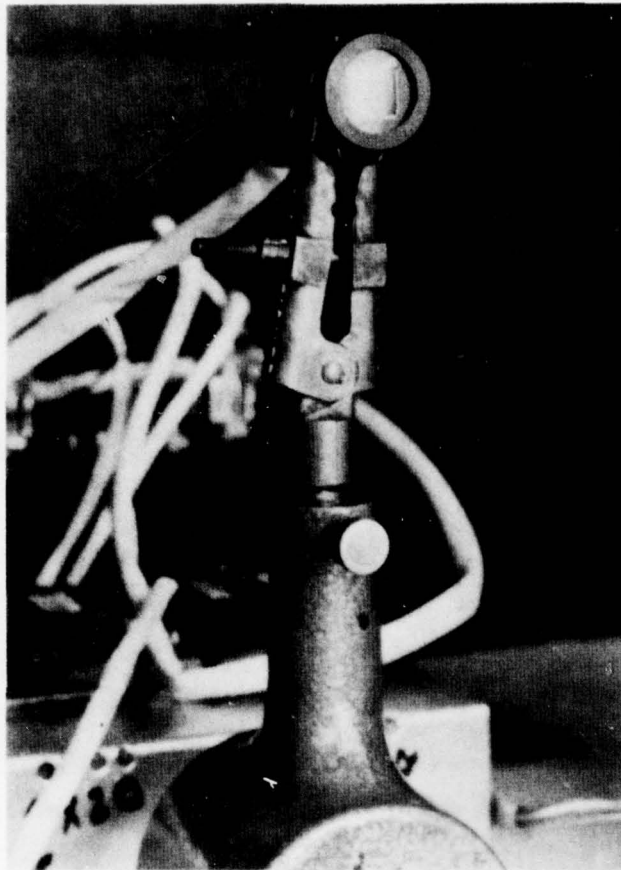
Figure 14.   The Four-Quadrant Cartesian
Photo-Diode

Using the characterization system, the data in figure 15 was collected. The measurement was made to determine deflector beam-aiming repeatability. Each spot marks the angular position of the energy centroid of the deflected beam in a sequence of reaiming the beam at the "same" spot. The process involved alternately erasing the grating with a saturation field normal to the direction of the dashed line and then switching to a lower drive field vector corresponding to the mid-graph position. The data indicates very accurate repeatability normal to the deflection radial. The standard deviation is 1/8 milli radian. Along the diffraction radial (i.e., the beam path from saturation to the hold position) the repeatability standard deviation is 2/3 milli radian. Because the beam divergence of this crystal was 1 1/4 milli radian, the data indicates the deflector "repeatability divergence" is much better than actual beam divergence. This data has been significant in the applications modeling and also demonstrates the type of measurements that are possible to make, now that this system is completed.

(MILLIRADIANS)

(MILLIRADIANS)

DIRECTION OF
APPLIED FIELD, I.E., THE
STRIPE ORIENTATION

DIRECTION
OF DEFLECTION
RADIAL
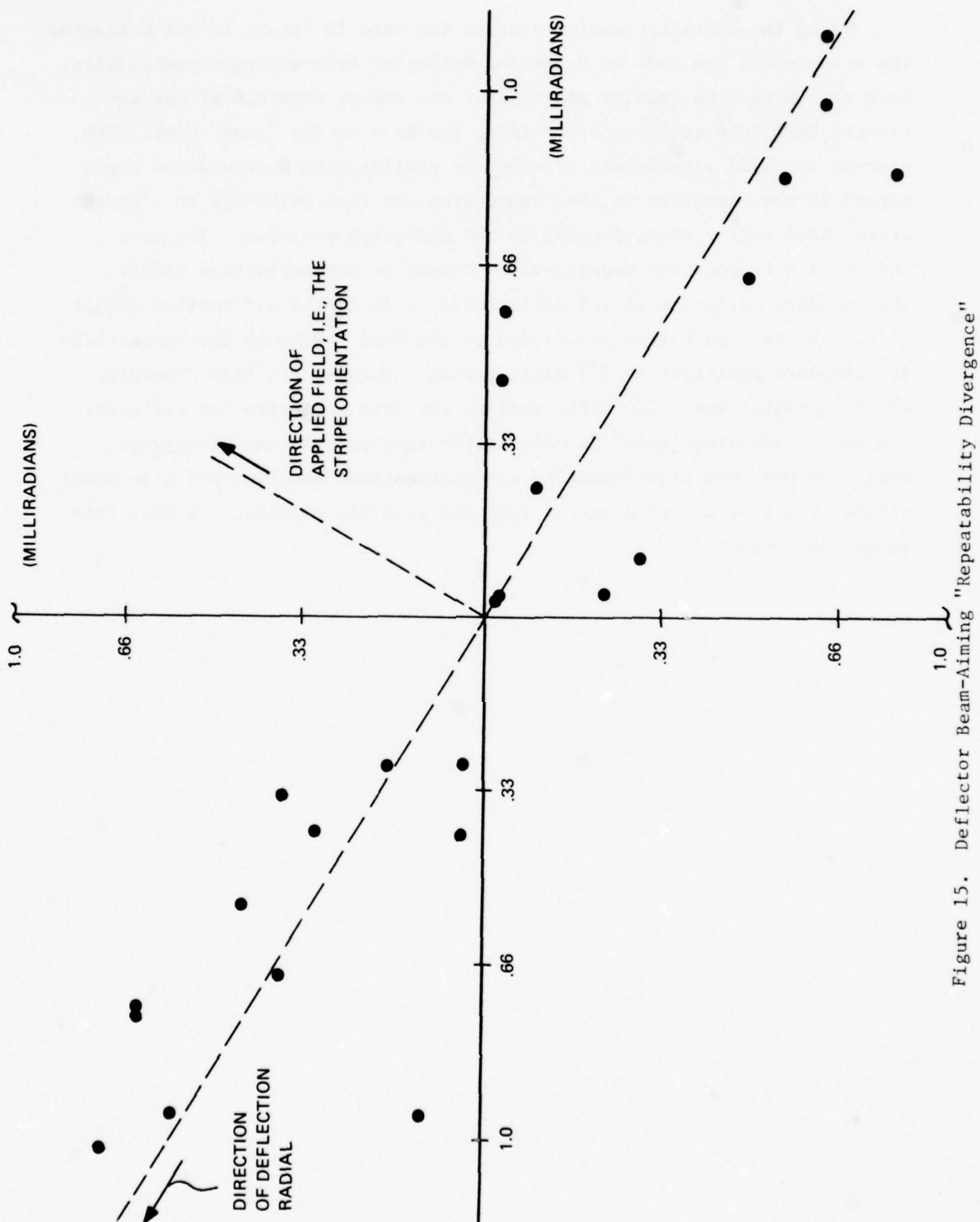
Figure 15. Deflector Beam-Aiming "Repeatability Divergence"

40

SECTION VI

SYSTEM ANALYSIS

A. Beam Divergence and Pointing Accuracy Analysis

1. Beam Divergence

Consider a laser and deflector located at some point 0 and a point T that is to be illuminated. The distance from 0 to T is the range R. Let U_T be the laser pulse energy and ρ be the radial distance from the center of the beam. If it is assumed that the energy distribution is gaussian, the energy density u at a distance ρ from the center of the beam will be given by

$$u = (U_T/2\pi\sigma_B^2)e^{-\rho^2/2\sigma_B^2}\, e^{-\sigma_A R}$$

where σ_B is the e^{-1} radius of the beam and σ_A is the atmospheric extinction coefficient.

This equation can be rewritten as

$$u = (2U_T/\pi R^2\delta^2)e^{-(2\theta^2/\delta^2\, +\, \sigma_A R)} \tag{1}$$

where δ is the beam divergence angle and is equal to $2\sigma_B/R$ and θ is equal to ρ/R. If we wish the beam energy density u to exceed a threshold value u_{TH}, then there will be a value of θ ($= \theta_{TH}$) at which u will be equal to u_{TH}.

$$(2U_T/\pi R^2\delta^2)e^{-(2\theta_{TH}^2/\delta^2\, +\, \sigma_A R)} = u_{TH} \tag{2}$$

41

Solving equation (2) for θ_{TH} we get

$$(2U_T/u_{TH}\pi R^2\delta^2) = e^{(2\theta_{TH}^2/\delta^2 + \sigma_A R)}$$

$$\ln(2U_T/u_{TH}\pi R^2\delta^2) = 2\theta_{TH}^2/\delta^2 + \sigma_A R$$

$$\theta_{TH}^2 = (\delta^2/2)(\ln(2U_T/u_{TH}\pi R^2\delta^2) - \sigma_A R) \tag{3}$$

To illuminate the largest cross section area at T, θ_{TH} must be maximized. To determine the value of δ which will maximize θ_{TH} the derivative of equation (3) is taken with respect to δ.

$$2\theta_{TH}(d\theta_{TH}/d\delta) = \delta(\ln(2U_T/u_{TH}\pi R^2\delta^2) - \sigma_A R - 1)$$

Using equation (3) to eliminate θ_{TH}

$$\frac{d\theta_{TH}}{d\delta} = \frac{2^{1/2}(\ln(2U_T/u_{TH}\pi R^2\delta^2) - \sigma_A R - 1)}{(\ln(2U_T/u_{TH}\pi R^2\delta^2) - \sigma_A R)^{1/2}} \tag{4}$$

Setting $d\theta_{TH}/d\delta = 0$ for $\delta = \delta_1$

$$\ln(2U_T/u_{TH}\pi R^2\delta_1^2) - \sigma_A R - 1 = 0$$

$$2U_T/u_{TH}\pi R^2\delta_1^2 = e^{(1 + \sigma_A R)}$$

$$\delta_1^2 = (2U_T/u_{TH}\pi R^2)e^{-(1 + \sigma_A R)} \tag{5}$$

42

θTHMAX, the maximum value of θ_{TH} is found by evaluating equation (3) at $\delta = \delta_1$.

$$\theta^2_{THMAX} = (\delta_1^2/2) \ (\ln \ (2U_T/u_{TH}\pi R^2\delta_1^2) - \sigma_A R)$$

Using equation (5) to eliminate δ, inside the ln expression

$$\theta^2_{THMAX} = (\delta_1^2/2) \ (1 + \sigma_A R - \sigma_A R)$$

or

$$\theta^2_{THMAX} = \delta_1^2/2$$

$$\theta_{THMAX} = \delta_1/2^{1/2} \tag{6}$$

Therefore the diameter of the maximum threshold area exceeds the diameter of the optimum beam divergence by a factor of $2^{1/2}$.

To find the beam divergence dependence of θ_{TH} we will first rewrite equation (5).

$$2U_T/u_{TH}\pi R^2 = \delta_1^2 e^{(1 + \sigma_A R)} \tag{7}$$

Next rewriting equation (2)

$$2U_T/u_{TH}\pi R^2 = \delta^2 e^{(2\theta^2_{TH}/\delta^2 + \sigma_A R)} \tag{8}$$

From equations (7) and (8)

$$\delta^2 e^{(2\theta^2_{TH}/\delta^2 + \sigma_A R)} = \delta_1^2 e^{(1 + \sigma_A R)}$$

43

or

$$\delta^2/\delta_1^2 = e^{(1 - 2\theta^2_{TH}/\delta^2)}$$

$$2 \ln \delta/\delta_1 = 1 - 2\theta_{TH}^2/\delta^2$$

$$\theta_{TH}^2 = (\delta^2/2) (1 - 2 \ln \delta/\delta_1)$$

Using equation (6) this becomes

$$\theta_{TH}^2 = \theta_{THMAX}^2 (\delta/\delta_1)^2 (1 - 2\ln \delta/\delta_1) \qquad (9)$$

This can also be written in terms of ρ which is equal to θ/R.

$$\rho^2_{TH} = \rho^2_{THMAX} (\delta/\delta_1)^2 (1 - 2\ln \delta/\delta_1)$$

In Figure 16 equation (9) is used to plot the ratio of the threshold angle to optimum threshold angle ($\theta_{TH}/\theta_{THMAX}$) vs the ratio of beam divergence angle to the optimum beam divergence angle (δ/δ_1). As δ/δ_1 decreases $\theta_{TH}/\theta_{THMAX}$ decreases with the intensity at the beam center increasing rapidly as the threshold angle collapses. As δ/δ_1 increases from 1, $\theta_{TH}/\theta_{THMAX}$ decreases slowly at first and then drops rapidly to zero at just over 1.64 where the intensity of the center of the beam drops below the threshold value.

2. Pointing Accuracy

The probability of exceeding the threshold energy at point T depends on the pointing accuracy. This probability is given by

$$P = 1 - e^{-\rho_{TH}^2/2\sigma_T^2} \qquad (10)$$

where σ_T is the pointing accuracy radius.

44

The miss probability is given by

$$Q = 1-P = e^{-\rho_{TH}^2/2\sigma_T^2} = e^{-R^2\theta_{TH}^2/2\sigma_T^2} \qquad (11)$$

or

$$Q = e^{-\theta_{TH}^2/2\alpha^2} \qquad (12)$$

where $\alpha = \sigma_T/R$

Consider equation (2)

$$u_{TH} = (2U_T/\pi R^2 \delta^2)e^{-\sigma_A R} e^{-2\theta_{TH}^2/\delta^2}$$

rewriting we get

$$u_{TH} = (2U_T/\pi R^2 \delta^2)e^{-\sigma_A R} e^{-2(\theta_{TH}^2/2\alpha^2)(2\alpha^2/\delta^2)} \qquad (13)$$

Using equation (12), equation (13) becomes

$$u_{TH} = (2U_T/\pi R^2 \delta^2) e^{-\sigma_A R} Q^{4\alpha^2/\delta^2} \qquad (14)$$

Solving equation (14) for Q we have

$$Q = (K\delta^2)^{(\delta/\alpha)^2/4} \qquad (15)$$

where

$$K = (u_{TH}\pi R^2/2U_T) e^{\sigma_A R}$$

We shall now determine the value of the beam divergences (δ) which minimize the miss probability (Q).

45

Taking the derivative of equation (15) with respect to δ we have

$$(dQ/d\delta) = (\delta/2\alpha^2) \ (K\delta^2)^{(\delta/\alpha)^2/4} \ (1 + \ln K\delta^2)$$

Setting the derivative equal to zero

$$K\delta_2^{\ 2} = e^{-1} \text{ where } \delta_2 \text{ minimizes } Q$$

or

$$(u_{TH}\pi R^2/2U_T) \ \delta_2^{\ 2} \ e^{\sigma_A R} = e^{-1} \tag{16}$$

Solving for δ_2 we get

$$\delta_2^{\ 2} = (2U_T/u_{TH}\pi R^2) \ e^{-(1 + \sigma_A R)} \tag{17}$$

We see from equations (5) and (17) that the value of the divergence angle (δ_1) that maximizes θ_{TH} is equal to the value of the divergence angle (δ_2) that minimizes Q.

To find the minimum value of Q evaluate equation (15) at $\delta = \delta_2$.

$$Q_{MIN} = (K \ \delta_2^{\ 2})^{(\delta_2/\alpha)^2/4}$$

or

$$Q_{MIN} = e^{-(\delta_2/\alpha)^2/4} \tag{18}$$

Equation (18) is plotted in Figure 17. The minimum miss ratio (Q_{MIN}) is approximately 0.1 at a divergence angle to pointing accuracy ratio

46

of 3 and decreases very rapidly as δ_2/α increases. Using equation (16) to eliminate K in equation (15) we have

$$Q^{4(\alpha/\delta)^2} = (\delta/\delta_2)^2 \, e^{-1}$$

or

$$Q = (\delta/\delta_2)^{(\delta/\alpha)^2/2} \, e^{-(\delta/\alpha)^2/4}$$

rewriting

$$Q = (\delta/\delta_2)^{-2(\delta/\delta_2)^2 \, (-(\delta_2/\alpha)^2/4)} \, e^{-(\delta_2/\alpha)^2 \, (\delta/\delta_2)^2/4} \qquad (19)$$

Using equation (18) to eliminate $-(\delta_2/\alpha)^2/4$ equation (19) becomes

$$Q = (\delta/\delta_2)^{-2(\delta/\delta_2)^2 \, \ln Q_{MIN}} \, Q_{MIN}^{(\delta/\delta_2)^2} \qquad (20)$$

Dividing both sides of equation (20) by Q_{MIN} we have

$$Q/Q_{MIN} = (\delta/\delta_2)^{-2(\delta/\delta_2)^2 \, \ln Q_{MIN}} \, Q_{MIN}^{(\delta/\delta_2)^2 - 1} \qquad (21)$$

Equation (21) is plotted in Figure 18 with the divergence angle to the optimum divergence angle ratio (δ/δ_2) as the variable and the minimum miss ratio Q_{MIN} as the parameter. As the minimum miss ratio decreases the miss ratio becomes more sensitive to variation of δ/δ_2 from 1.

B. Signal to Background Noise in Ladar Systems

Consider a laser system as shown in Figure 19. An expression for signal to noise will be used to determine the transmitted power requirements
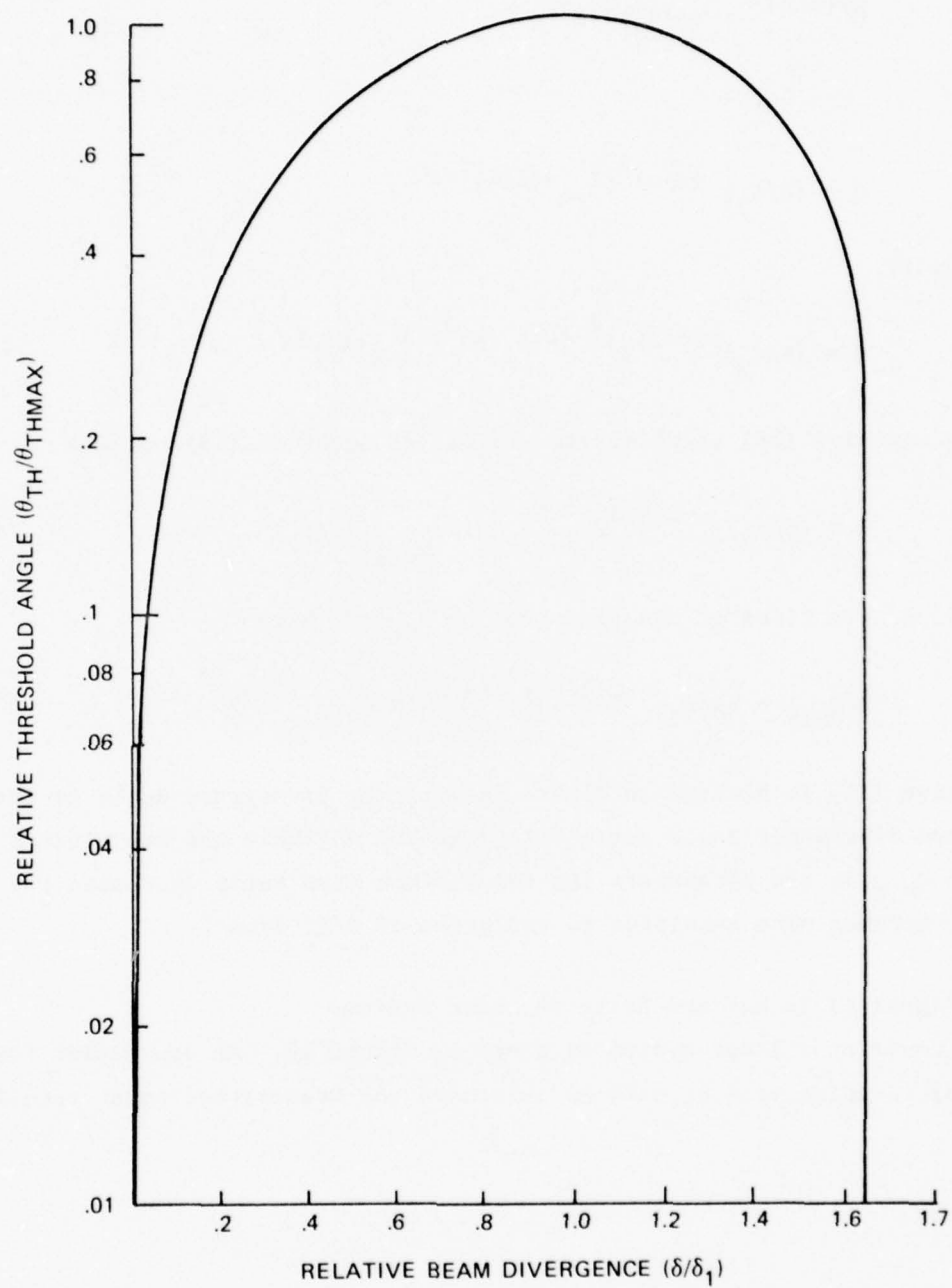
Figure 16. Ratio of the Threshold Angle to Optimum Threshold Angle vs. Ratio of Beam Divergence Angle to Optimum Beam Divergence Angle
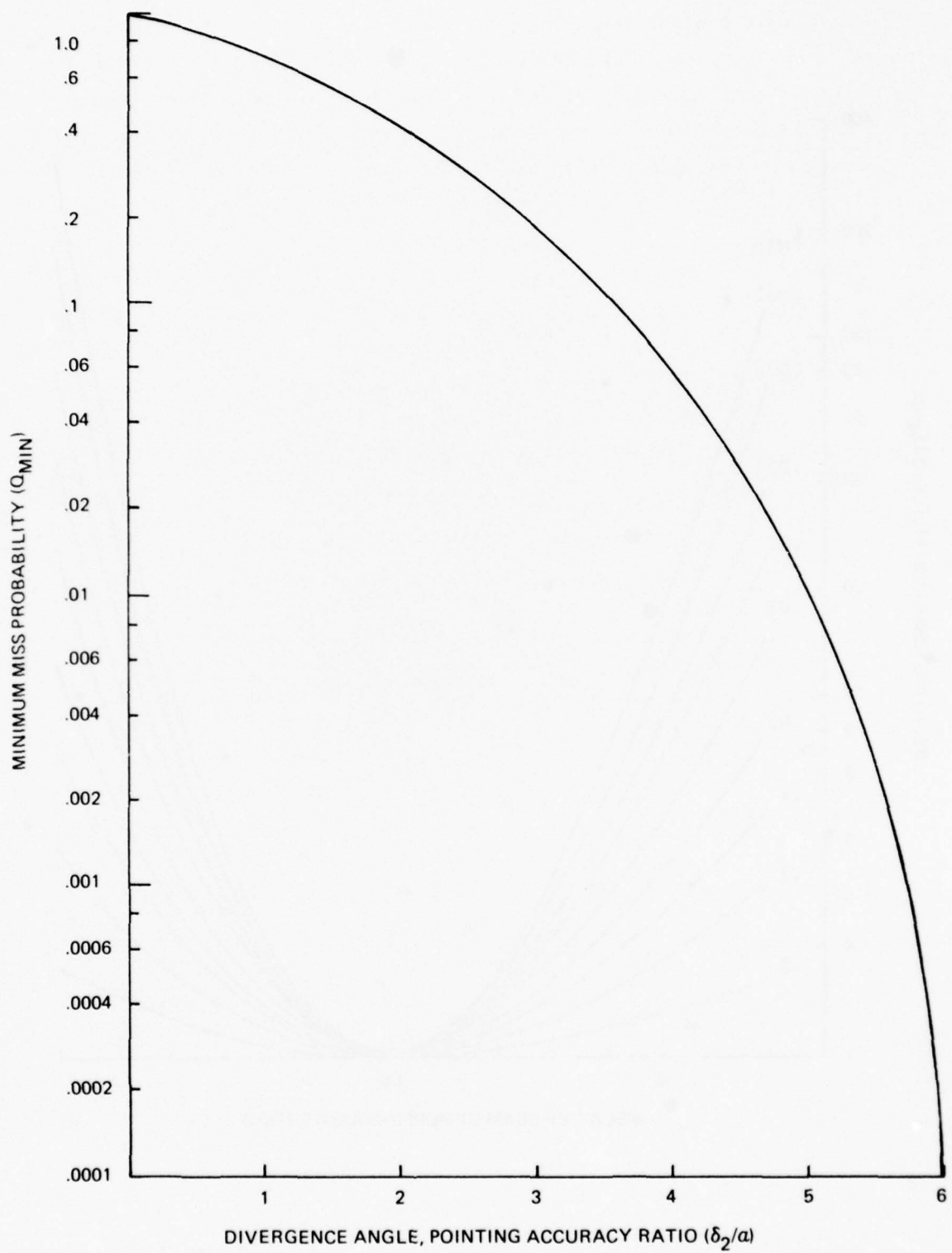
48

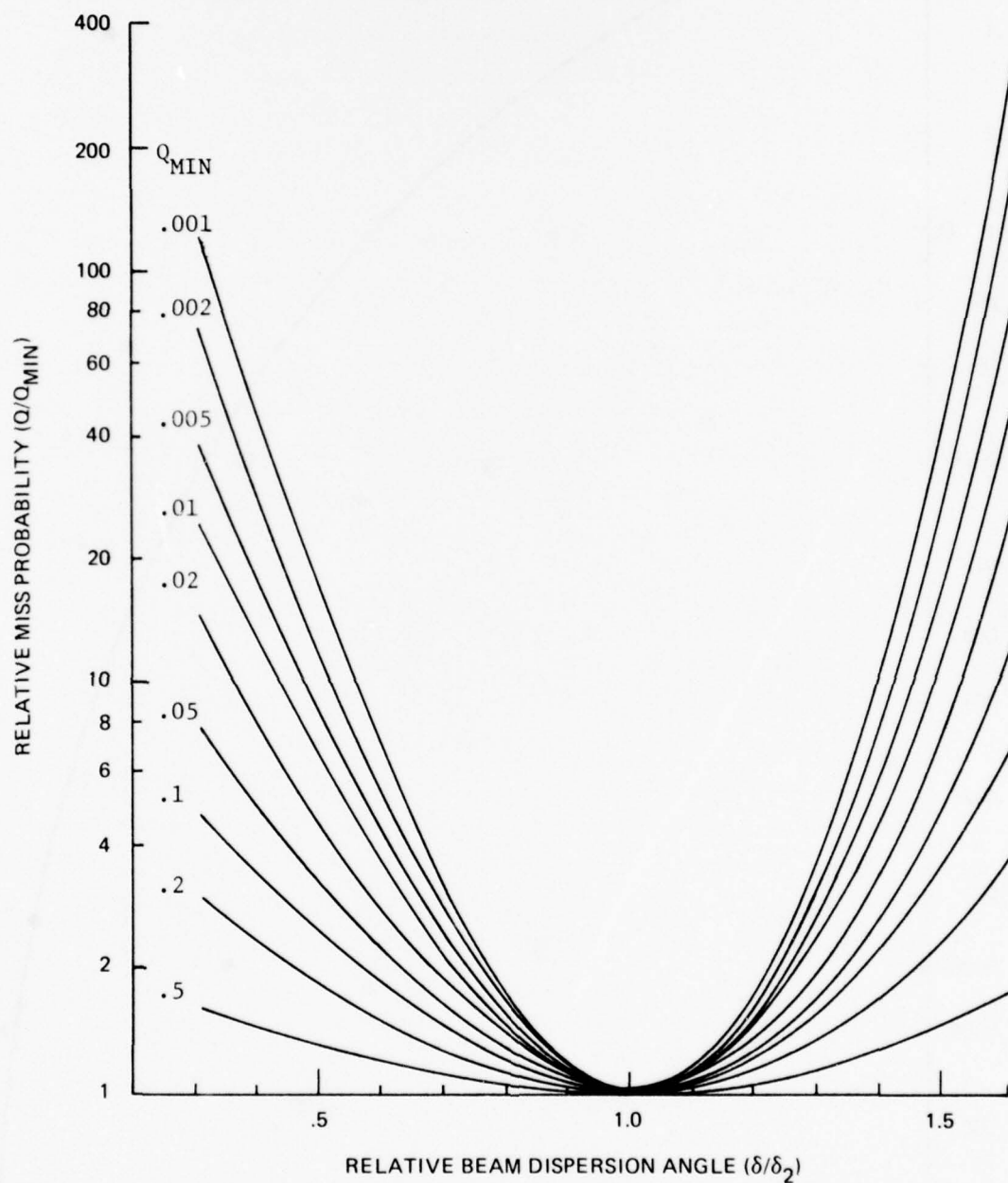Figure 17. Minimum Miss Ratio to Pointing Accuracy Ratio

49

Figure 18. Divergence Angle Ratio as Variable; Minimum Miss Ratio as Parameter

50

for various target cross sections and various classes of receivers. The transmitted power requirement is pertinent for two reasons:

1) Form fit lasers for avionics applications are average power limited; high energy per pulse is traded for high pulse rates.

2) The transmitted power requirement may be difficult to meet because of the limitations imposed by various optical components in the transmitter; specifically, the deflector may not handle the power level.

1. Background Noise

One way to estimate the noise in an optical signal is to assume that the collector part of the receiver is large enough to make the solar radiation scattered by the atmosphere the dominant source of noise, (as opposed to detector or amplifier noise). In a pulsed laser system, the receiver integrates the background noise for a certain period of time. For example a TV camera operating at 30 frames/seconds integrates background noise for 33 milliseconds. The value of background 1.06 micrometer radiance can be estimated from data in Low Tran. Since the spectral radiance depends on the position of the sun, the zenith value ranges from 21 $W\ m^{-2}\ sr^{-1}\ \mu m^{-1}$ for a 77° sun elevation down to .047 $W\ m^{-2}\ sr^{-1}\ \mu m^{-1}$ for a 15° sun elevation. The highest value 21 $W\ m^{-2}\ sr^{-1}\ \mu m^{-1}$ will be used since it represents the most difficult condition of background noise. The AM1 solar constant, which corresponds to direct sunlight, is 600 $W\ m^{-2}\ \mu m^{-1}$ at 1.06 μm wavelength.

The background noise energy expression is

$$N = p\Omega_c \quad A_c \quad F \quad \Delta T$$

51

with

p = Background radiance, $W\ m^{-2}\ sr^{-1}\ \mu m^{-1}$

Ω_c = Receiver Field of view, sr

F = Spectral filter passband, μm

ΔT = Integration time associated with the receiver

A_c = Collector area

The collector area drops out of the S/N expression. The value of Ω depends on both the field of view and the type of detector. For example, the FOV could be 2π sr and the detector could be a single photodiode; Ω would then be 2π. The detector could be an nxn array of photodiodes, and then $\Omega = 2\pi/n^2$. Each diode in the array sees only its small portion of the FOV. The integration time, ΔT, also depends on the type of detector. The filter width must be chosen to accommodate the doppler shifts due to target motion. For satellites and ICBM's $F \geq 0.02\ \mu m$ since their relative velocity can be large. For, aircraft, $F \sim 0.002\ \mu m$ is probably adequate. Thus;

$$N = 42\Omega_c\ A_c\ \Delta T\ mJ$$

2. Signal Energy

The signal energy depends on the transmitted energy E_o, transmitted beam divergence, Ω_T, the atmospheric transmission characteristics, T, the target cross section σ, the receiver cross section A_c, and the separation (range) R, of transmitter, receiver and target. An expression for signal energy, S, for small targets is

$$S = \frac{T^2\ E_o\ A_c\ \sigma}{R^4 \Omega_T}$$

This expression assumes negligible beam break-up due to atmospheric effects. This expression can be combined with the noise expression to obtain the ratio of signal to noise:

$$\frac{S}{N} = \frac{E_o \, T^2 \sigma}{42\Omega_R \quad \Delta T \quad R^4 \Omega_T} \tag{2}$$

with R in meters, E_o in millijoules, and σ in m^2/sr. It is assumed that the transmitted pulse width is much shorter than the integration time ΔT, so that in a time ΔT all of the target return energy is captured.

The required signal-to-noise for a tailwarning system or a target designating system depends on the details such as false alarm rate and probability of kill. Even though precise values for S/N are not known at the time of this writing, let $S/N \geq 10$ for definiteness.

Thus (2) becomes

$$\frac{E_o \, T^2 \, \sigma}{42\Omega_R \quad \Delta T \quad R^4 \Omega_T} \geq 10 \tag{3}$$

with this condition E_o can be calculated for various ranges, target cross sections, beam divergences and receivers. Note the atmospheric term T can be written $T^2 = e^{-2\alpha R}$ and α can be estimated from data in Low Tran. For low altitudes, α is dominated by aerosols: $\alpha = 8.77 \times 10^{-2}$ km^{-1} for clear air and $\alpha = 4.47 \times 10^{-1}$ km^{-1} for hazy air. For simplicity, the sample calculations will use $\alpha = 0.1$ km^{-1}.

53

Expression (3) is then

$$\frac{E_o \sigma \; e^{-0.2R/10^3}}{\Omega_R \; \Delta T \; R^4 \; \Omega_T} \geq 420 \text{ mj} \qquad (4)$$

This can be rewritten

$$E_o \geq (420 \Omega_T \Omega_R \; \Delta T) \cdot \frac{R^4 \; e^{0.2R/10^3}}{\sigma} \qquad (5)$$

The first term on the right can be made small either by using a transmitted beam with as small a divergence as possible, or by using a narrow FOV receiver (with many elements), or by using a fast receiver. The second term is set more or less by the specifics of the mission.

Consider the term

$$\Omega_T \; \Omega_R \; \Delta T$$

The filter, F, was chosen to match the expected doppler shifts in the light returning from the target: $F = 20 \text{ Å}$. If the transmitted laser pulse is formed by superposing various laser modes with modelocking or other techniques, very short laser pulses can be formed. Imagine that all of the modes contained in a pulse so formed have a wavelength within $\Delta \lambda = \pm 5 \text{ Å}$ of some center wavelength. The return pulse will get through the filter. The width of a pulse that can be formed using the modes within $\pm 5 \text{ Å}$ is calculated by using

$$\left| \frac{\Delta f}{f} \right| = \left| \frac{\Delta \lambda}{\lambda} \right|$$

54

The shortest pulse is about three picoseconds. Very few detectors can respond in this time frame. Electronic streak cameras are one notable exception; very sophisticated range gated systems are another. The laser bandwidth appears to exceed the bandwidth of most detector-filter combinations. Even with a detector with picosecond response time the data rate may cause some interesting and unusual data processing problems.

Many detectors such as photovoltaic or photoconductive pn devices exist which operate in nanoseconds. These speeds are commensurate with nanosecond laser pulses (which are available from form fit lasers). Such detectors can be used to give ranges to ± 10 cm or better. Range rates can be calculated to reasonable accuracies from such range measurements.

The class of detectors which image the field of view include CCD, CID arrays and TV tubes. The serial data streams from these devices gives rise to long integration times: tens of milliseconds. Consequently, large amounts of background noise energy accumulates unless range gating is used. Range gating requires some knowledge of the target range to be effective. However these detectors are useful for generating angular beam control signals. Furthermore the noise energy is reduced by the small portion of the FOV that each element in the array sees. Thus the product

$$\Omega_R \; \Delta T$$

is about the same for single element high speed detectors, $(1 \times 10^{-8}$ sec$)$, and arrays $(10^{-6} \times 10^{-2}$ sec$)$.

For this reason, we will consider the use of the deflector as a part of the receiver using the deflector to provide angular discrimination for a high speed quadrant detector. This $\Omega_R \; \Delta T$ product with this combination ought to be $10^{-6} \times 10^{-8} = 10^{-14}$ sec. which ought to offset insertion losses.

55

This discussion, incidently, has assumed uniform background noise. At very low background noise levels the photons arrive in bunches and this will require a more elaborate analysis. The assumption of background noise limited operation is questionable when size limits are placed on the optic apertures.

Consider as an example a $\sigma = 1 \ m^2/sr$ target at a range of 10 km:

$$\frac{R^4 e^{0.2R/10^3}}{\sigma} = 7.4 \times 10^{16} \ m^2$$

and so

$$E_o \geq 3 \times 10^{19} \ \Omega_T \ \Omega_R \ \Delta T \ \text{millijoules} \tag{6}$$

Let $\Omega_T \sim 10^{-8}$ sr which corresponds to diffraction limited beam divergence with an exit aperture of 1.2 cm. It is also consistent with the magnitude of RMS tracking errors that may be encountered. With $\Omega_T = 10^{-8}$ sr

$$E_o \geq 3 \times 10^{11} \ \Omega_R \ \Delta T \ \text{m joules}.$$

The payoff in detector design is self evident.

C. Deflector Systems

If a single deflector could be used both for deflecting the transmitted laser beam and scanning for the return reflection, systems requirements would be relieved the difficult task of coordinating two separate deflector elements. A necessary characteristic of the deflector element to meet this requirement is that the reflected beam is diffracted through the same angle as the transmitted beam. It can reasonably be argued that this is the expected behavior of grating diffraction. However, it was important that this expectation be experimentally verified. This experiment is diagrammed

56
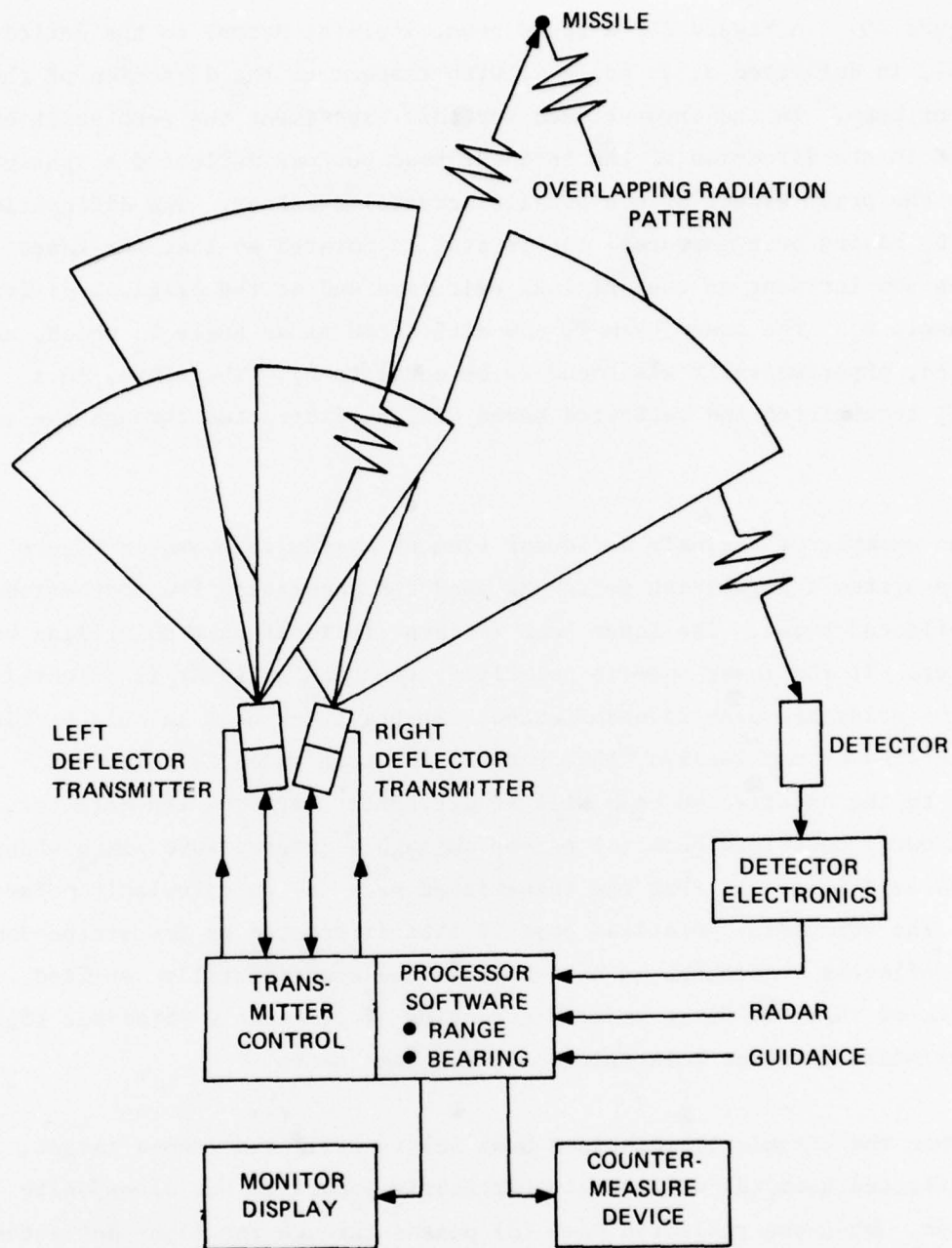
The overlapping radiation pattern insures detection in the blind spot. A processor computes range and bearing for the countermeasure device and provides a display signal, transmitter control signal and deflector control signal.

Figure 19. Active Tail Warning System

57

in Figure 20. In Figure 20a a laser beam, incident normal to the deflector crystal, is deflected at an angle θ_1 with respect to the direction of the incident beam. In the crystal used for this experiment the zero order beam was not in the direction of the incident beam but was deflected slightly due to the prism effect of non-parallel crystal surfaces. The diffraction angle θ_1 having been measured, the crystal is rotated so that the laser beam is now incident on the original exit face and at the original diffraction angle θ_1. The laser beam is now diffracted at an angle θ_2 which, as expected, experimentally was found to be equal to θ_1. Therefore, in a system, transmitted and reflected beams will be diffracted through the same angle.

An example of a single deflector element system is shown in Figure 21. In this system a polarizing system is used for separating the transmitted and reflected beams. The laser beam is first incident on a polarizing beam splitter. If the laser beam is polarized, the beam splitter is oriented so that the polarized beam is undeflected. If the laser beam is only partially polarized or unpolarized, that part of the beam which is polarized normal to the undeflected beam will be deflected away from the detector. The linearly polarized beam (a) passes through a quarter wave plate whose optical axis is set so that the transmitted beam (b) is circularly polarized. The circularly polarized beam is then diffracted by the stripe-domain light deflector. Although it has not yet been experimentally verified, it is expected that the first order diffraction of circularly polarized light will maintain circular polarization of the same sense.

When the circularly polarized beam (c) is reflected from a target, the reflected beam (d) will remain circularly polarized but of opposite rotation. When the reflected beam (d) passes through the light deflector, the diffracted angle will be the same as for the transmitted beam, so that the beam (e) will be parallel to the transmitted beam (b). Since the beam is now of opposite rotation, linearization by the quarter-wave plate will

yield a beam (f) whose plane of polarization is normal to that of beam (a). Therefore, the return beam will be deflected by the polarizing beam splitter to the detector. Polarizing systems should also have the advantage of increasing the signal to background noise ratio.
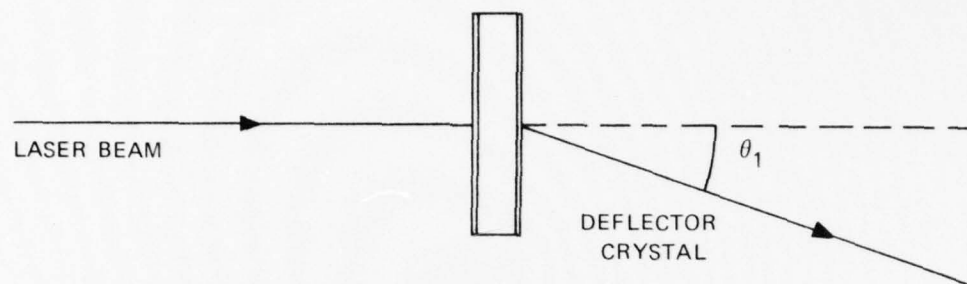
20a.
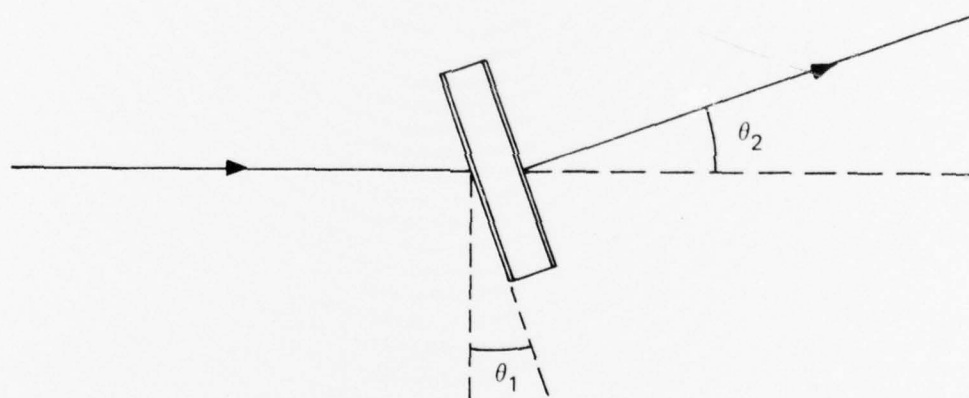
20b.

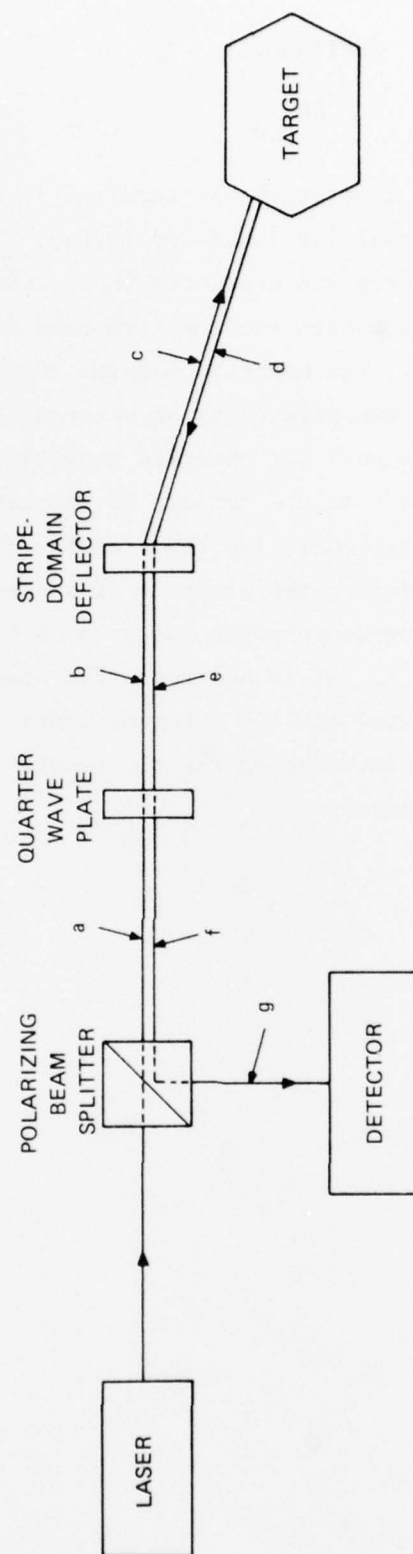Figure 20.   Reflected Beam Diffracted Through the Same Angle as Transmitted Beam

Figure 21.   Single Deflector Element Transmitter - Receiver System

61

SECTION VII

EuO

    A search of the available literature has resulted in the identification of at least one candidate material for 3.8μm and 10.6μm. The candidate is europous oxide. Since this survey was conducted there have been additional experimental results. Magnetic domain studies have been conducted by using an IR vidicon and a TV monitor. The magnetic domains exhibited appreciable directionality and were easily manipulated by an externally applied magnetic field. Sharp domain boundaries were not observed possibly due to a canting of the magnetization with respect to the surface of the crystal. Anomalous absorption of IR radiation at extremely low temperatures ($\sim 20^{\circ}$K) was observed. This phenomenon is due to the presence of a donor level which is above the conduction band at low temperature but crosses below it when the temperature is increased to 50°K. It is believed this absorption can be decreased by annealing the crystal at 1400°C for 60 hours in an oxygen-rich atmosphere. These results are encouraging for the eventual development of a EuO stripe-domain light deflector.

SECTION VIII

CONCLUSIONS AND RECOMMENDATIONS

A. Introduction

It is the central important conclusion of this program that there is a high probability that large, high-quality, high-efficiency bismuth rare-earth light deflector crystals can be developed and that there are viable uses for systems using this technology. It is our recommendation that research and development for this technology be continued and expanded so that the technology becomes available in a timely manner.

B. Optical Absorption Measurements

Although the present absorption measurement is sufficient for film evaluation it is not useful for melt development or melt tuning. The problem is the excessive turn-around time of 2 days; one day for data collection and one day for data reduction and calculation. Crystals cannot be grown with consistent characteristics at this low a rate due to many factors, one of which is melt volatization. Another problem which should be addressed is experimental errors caused by the excessive sample handling and moving which is required in the present instrumentation. In view of these problems we recommend an improvement program for the optical absorption measurement which includes new equipment and modified procedures.

The improved optical absorption measurement system would be based on a digital output spectrophotometer. This would allow direct output into a computer and eliminate the tedious and time-consuming hand data reduction. This would also make practical analyzing other variables. For example, presently, fringe amplitude is extracted during the computer calculation but is not obtained during data reduction because of time considerations. A digital spectrophotometer will allow rapid acquisition of average transmission and reflection coefficients along with interference fringe

63

amplitude, fringe spacing, **fringe modulation** amplitude, and fringe modulation spacing, all as a function of wavelength.

Another important advancement would be the development of a new sample holding fixture. One of the features of this fixture would be once-only mounting of the garnet film sample. The fixture would incorporate a rotating stage for in-plane angle changes. Changes between the transmission, reflection, and reference configurations would also be done by movable fixtures. One of the advantages of this new fixture would be to increase repeatability so that the present redundant reference measurement could be eliminated. In addition, the rotating stage could be used to search for the optimum in-plane angle, thereby eliminating approximately 85% of the required data. A motorized rotating stage would be useful for this purpose. Other features which might be included are saturating magnetic field coils to eliminate and measure diffraction loss, and temperature control. It might also be possible, by incorporation of the proper polarizers and analyzers, to obtain Faraday rotation data from this instrumentation.

Along with improved instrumentation a number of improvements would be made in data reduction and calculations. Of primary importance for taking advantage of digital outputs for time-saving is the development of programming to do the data handling and reduction. This should reduce the time requirements by at least 95%. In addition, programming could be developed to automate data presentation. It is also expected that improvements would be made in the calculation process. For example, degree of coherence could be incorporated into the film multiple reflection calculation made possible by easily and rapidly acquired fringe amplitude data. This would increase the accuracy of the absorption calculation and give some indication of surface and film-substrate interface quality.

This recommended program should reduce optical absorption turn-around time to less than two hours thereby permitting timely development of high-quality, high-efficiency, garnet deflector films.

C. Film growth and facilities

Progress over the past years has included Faraday rotation increase through bismuth substitution, strain-free growth that eliminated crystal cracking and peeling, eliminating flux adhesion problems, reducing optical absorption, and increasing deflector resolution through defect reductions. Further development is primarily a refinement activity highly dependent on precise and flexible control of the furnace temperature and gradients and a dust-free operating environment. With this in mind, new crystal growing facilities are being pursued. Planned is a Class 100 room with microprocessor controlled three-zone furnaces. Refinement activities planned include:

1) more accurate temperature control to allow producing homogeneous crystals with spin-off digital characterization studies.

2) being able to control and tailor thermal gradients with the three zone furnaces to enable growing crystals in the present melts without spontaneous nucleation. This will provide lower defect densities, further increasing deflector resolution, and allow longer growth periods permitting production of thicker samples.

3) using the mass memory capability of the microprocessor, accurate thermal history of each crystal growth cycling and each melt's cumulative thermal history to provide higher experimental yield, consistency, and allow effective melt volitization replenishment. Of particular importance, rapid determination of why one crystal is better than another will be significantly aided by the availability of this type and detail of data.

4) operating in the class 100 environment to further reduce defect and beam divergence problems. The increase in resolution using the present laminar hood furnace indicates that this is a valuable approach.

The overall strategy will be to constrain enough variables and eliminate enough masking problems to allow measurement, study, and elimination of the more subtle problems.

66